Factors Determining the Impact of Aerosols on Surface Precipitation from Clouds: An Attempt at Classification

A. P. KHAIN, N. BENMOSHE, AND A. POKROVSKY

Department of Atmospheric Sciences, The Hebrew University of Jerusalem, Jerusalem, Israel

(Manuscript received 14 May 2007, in final form 12 October 2007)

ABSTRACT

The simulation of the dynamics and the microphysics of clouds observed during the Large-Scale Biosphere–Atmosphere Experiment in Amazonia—Smoke, Aerosols, Clouds, Rainfall, and Climate (LBA–SMOCC) campaign, as well as extremely continental and extremely maritime clouds, is performed using an updated version of the Hebrew University spectral microphysics cloud model (HUCM). A new scheme of diffusional growth allows the reproduction of in situ–measured droplet size distributions including those formed in extremely polluted air. It was shown that pyroclouds forming over the forest fires can precipitate. Several mechanisms leading to formation of precipitation from pyroclouds are considered.

The mechanisms by which aerosols affect the microphysics and precipitation of warm cloud-base clouds have been investigated by analyzing the mass, heat, and moisture budgets. The increase in aerosol concentration increases both the generation and the loss of the condensate mass. In the clouds developing in dry air, the increase in the loss is dominant, which suggests a decrease in the accumulated precipitation with the aerosol concentration increase. On the contrary, an increase in aerosol concentration in deep maritime clouds leads to an increase in precipitation. The precipitation efficiency of clouds in polluted air is found to be several times lower than that of clouds forming in clean air. A classification of the results of aerosol effects on precipitation from clouds of different types developing in the atmosphere with high freezing level (about 4 km) is proposed. The role of air humidity and other factors in precipitation's response to aerosols is discussed. The analysis shows that many discrepancies between the results reported in different observational and numerical studies can be attributed to the different atmospheric conditions and cloud types analyzed.

1. Introduction

Observations and numerical studies indicate that atmospheric aerosols affect cloud microphysical structure and precipitation formation. An increase in the concentration of submicron-size aerosol particles (APs) serving as cloud condensation nuclei (CCN) increases the concentration and decreases the size of droplets (e.g., Rosenfeld and Lensky 1998; Ramanathan et al. 2001; Andreae et al. 2004). Numerical models with accurate spectral-bin microphysics can reproduce observed drop–aerosol concentration dependencies (e.g., Segal and Khain 2006; Kuba and Fujiyoshi 2006).

Recent numerical studies (e.g., Khain et al. 2003, 2004, 2005; Wang 2005; Lynn et al. 2005a; Teller and Levin 2006; van den Heever et al. 2006; Lee et al. 2008) and observations (Koren et al. 2005) reported aerosol-induced invigoration of deep convection, that is, an increase in convective updrafts and downdrafts as well as in horizontal and vertical cloud size. At the same time, the effect of aerosols on precipitation still remains a challenging problem. There is no agreement between the results of different studies as regards the quantitative and even the qualitative evaluation of aerosol effects on precipitation. Most observational (Albrecht 1989; Rosenfeld 1999, 2000; Rosenfeld and Woodley 2000; Givati and Rosenfeld 2004; Jirak and Cotton 2006; Borys et al. 2000) and numerical (e.g., Feingold et al. 2005) studies show that aerosols tend to suppress precipitation in stratocumulus and small cumulus clouds. The aerosol-induced invigoration of deep convection is often interpreted to mean that aerosols increase precipitation from deep convective clouds. Such an increase was reported, for instance, in some observa-

Corresponding author address: Prof. Alexander Khain, Department of Atmospheric Sciences, The Institute of Earth Science, Givat Ram, The Hebrew University of Jerusalem, Jerusalem, Israel.
E-mail: khain@vms.huji.ac.il

DOI: 10.1175/2007JAS2515.1

tional and numerical studies (e.g., Ohashi and Kida 2002; Shepherd and Burian 2003; Wang 2005; Lynn et al. 2005a,b).

The classification of clouds as shallow or deep, depending on their response to aerosols, is, however, not exact. Khain et al. (2004, 2005), Lynn et al. (2007), and, more recently, Tao et al. (2007) showed that an increase of atmospheric aerosols can either decrease or increase the precipitation from deep convective clouds and convective systems, depending on the environmental conditions. For instance, Lynn et al. (2007) showed that the aerosol-induced precipitation decrease in stratocumulus orographic clouds reported by Givati and Rosenfeld (2004) in California took place only in comparatively dry air, while an increase in the air humidity can change the sign of the aerosol effect. As a result, the effect of aerosols on precipitation in orographic clouds can change from season to season or even from night to day. Khain et al. (2005), Lynn et al. (2005b), and Tao et al. (2007) found that the increase in precipitation from deep convective clouds with an increase in AP concentration took place mainly under wet environmental conditions, while the precipitation decrease was found in a dry unstable atmosphere (e.g., Khain et al. 2004). Thus, aerosol effects on precipitation can be considered only in combination with other environmental factors, such as humidity and atmospheric instability (Williams et al. 2002).

Precipitation at the surface often represents a small difference between two large terms: the generation of condensate G by diffusional growth, and its loss L by drop evaporation and ice sublimation. This fact imposes strict demands on the accuracy of the calculation of both generation and loss of condensate to evaluate the magnitude and the sign of aerosol effect on precipitation. Even a 10% error in the calculation of, say, evaporation, may lead to a 100% error of the evaluated precipitation amount. This is one of the reasons for flagrant errors in precipitation prediction by the state-of-the-art models. Simulation of aerosol effects on precipitation requires models with an accuracy of an order of magnitude higher than that required for precipitation calculation, because such models should reveal precipitation changes that can be as small as 10%–30% of the "mean" value. Thus, some discrepancies in numerical results concerning aerosol effects on precipitation can be attributed to the use of numerical models with quite different accuracies in their calculation of moisture and heat budget items (Lynn et al. 2005a,b; Lynn et al. 2007; Li et al. 2007, manuscript submitted to *J. Atmos. Sci.,* hereafter LiTa). In the present study, we focus on another aspect of the problem—when the discrepancies can be attributed to different atmospheric conditions or different cloud types included in the studies.

Both the generation and the loss of the hydrometeor mass depend on the shapes of droplet size distributions (DSDs) and other hydrometeors. At the same time, the number of observational studies allowing a detailed comparison of DSD evolution with height under different aerosol conditions is quite limited. The research flights performed during the Large-Scale Biosphere–Atmosphere Experiment in Amazonia—Smoke, Aerosols, Clouds, Rainfall, and Climate (LBA–SMOCC) campaign at 1900 UTC 1 October 2002 (10°S, 62°W) and 1900 UTC 4 October 2002 (10°S, 67°W; Andreae et al. 2004) provided unique information concerning the microstructure of convective clouds arising under different aerosol concentrations. During these flights, the DSD in clouds developing in clean ("green ocean"; GO clouds), polluted ("smoky"; S clouds), and extremely polluted ("pyroclouds"; P clouds) air were measured in situ at different heights, up to 4200 m above the ground.

Pyroclouds represent an extreme form of smoky clouds that are fed directly by the smoke and the heat of fires. These clouds in the Amazon have been observed to reduce the cloud droplet size beyond what had been considered possible until now (Andreae et al. 2004). Forest fires in North America have been found to transport APs from the boundary layer to the stratosphere at least up to 16 km (Jost et al. 2004; Fromm and Servranckx 2003). These clouds affect tropospheric concentrations of trace gases and APs several thousand kilometers away (Forster et al. 2001; Wotawa and Trainer 2000). Such emissions substantially affect the upper-tropospheric and lower-stratospheric radiation balances (e.g., Cofer et al. 1996).

The purpose of the study is twofold: (i) to reproduce the microphysical characteristics of the developing GO, S, and P clouds using a spectral microphysics cloud model, and (ii) to analyze the mechanisms by which aerosols affect the precipitation formation in these clouds, as well as in extremely continental and maritime ("blue ocean") clouds. These convective clouds are analyzed here together because all of them have a high freezing level of 4–4.5 km above the ground. Convective clouds that have a low freezing level do not produce warm rain, and aerosol effects on precipitation of such clouds require special consideration. The clouds chosen for the analysis in this paper cover a wide range of aerosol and thermodynamic conditions: from clean, wet, and comparatively stable maritime ones observed (M clouds) during the 1974 Global Atmospheric Research Program (GARP) Atlantic Tropical Experiment (GATE-74; Warner et al. 1980; Ferrier and Houze 1989; Khain et al. 2005), to extremely dry, unstable, and

dirty conditions typical of summertime Texas clouds (T clouds; Rosenfeld and Woodley 2000; Khain et al. 2001b; Khain and Pokrovsky 2004). The GO and S clouds observed during the SMOCC campaign hold an intermediate position between these two extremes.

The description of the cloud model is presented in section 2. To reproduce the observed vertical broadening of the DSD, an especially accurate treatment of drop nucleation and diffusional growth is required. The spectral microphysics Hebrew University Cloud Model (HUCM; Khain et al. 2004) has been improved accordingly. We describe the experimental design in section 3. The microphysics of clouds observed in the SMOCC campaign, as can be seen from numerical results, is presented in sections 4 and 5. An analysis of aerosol effects on precipitation formation in deep convective clouds with a high freezing level is presented in section 6. This analysis is carried out with the help of mass, heat, and moisture budgets. The concept allowing the classification of aerosol effects on such clouds is proposed in section 7. The summary and conclusions are presented in section 8.

2. The model description

Because the basic components of the 2D nonhydrostatic HUCM are described by Khain and Sednev (1996) and Khain et al. (2004, 2005) in detail, we focus here on the model improvements. The model microphysics is based on the solution of a kinetic equations system for the size distribution functions of water drops, ice crystals (plate, columnar, and branch types), aggregates, graupel, and hail/frozen drops, as well as atmospheric APs. Each size distribution is described using 33 mass-doubling bins. Graupel is defined as rimed hydrometeors with the bulk density of 0.4 g cm^{-3}. Graupel forms as a result of water–ice collisions if the resulting particle has a melted radius exceeding 100 μm. Hail (or frozen drops) has a density of 0.9 g cm^{-3}. In the model, hail forms by freezing raindrops with radii exceeding 100 μm, or as a result of graupel–water drop collisions if the graupel radius exceeds 1000 μm and the liquid water content (LWC) exceeds 3 g cm^{-3}. With such LWC, the mass of the graupel particles approximately doubles during one collisional time step (10 s), so the resulting particles can be assigned to the category of hail. This value of LWC was considered typical for the beginning of wet growth of hail by Dennis and Musil (1973) and Smith et al. (1999). Frozen drops with a radius below 100 μm are assigned to the category of platelike crystals having the density of pure ice (0.9 g cm^{-3}). The model is specially designed to take into account the effects of atmospheric APs on the cloud microphysics and dynamics, as well as on precipitation formation. The initial (at $t = 0$) CCN size distribution is calculated (see Khain et al. 2000) using the empirical dependence

$$N = N_o S_1^k, \tag{1}$$

where N is the concentration of activated AP (nucleated droplets) at the supersaturation S_1 (%) with respect to water, and N_o and k are the measured constants. At $t > 0$ the prognostic equation for the size distribution of nonactivated APs is solved. Using the value of S_1 calculated at each time step, the critical AP radius is calculated according to the Kohler theory. The APs with radii exceeding the critical value are activated and new droplets are nucleated. The corresponding bins of CCN size distributions become empty.

The primary nucleation of ice crystals of each type is performed within its own temperature range, following Takahashi et al. (1991). The ice nuclei activation is described using the empirical expression suggested by Meyers et al. (1992) and applying a semi-Lagrangian approach (Khain et al. 2000), thus allowing the utilization of the diagnostic relationship in the time-dependent framework. The secondary ice generation is described according to Hallett and Mossop (1974). The rate of drop freezing is described following the observations of immersion nuclei by Vali (1994, 1975) and of homogeneous freezing by Pruppacher (1995). The diffusional growth/evaporation of droplets and the deposition/sublimation of ice particles are calculated using analytical solutions for supersaturation with respect to water and ice (see below). An efficient and accurate method of solving the stochastic kinetic equation for collisions (Bott 1998) is extended to a system of stochastic kinetic equations calculating water–ice and ice–ice collisions. The model uses height-dependent drop–drop and drop–graupel collision kernels following Khain et al. (2001a) and Pinsky et al. (2001). Ice–ice collection rates are assumed to be temperature dependent (Pruppacher and Klett 1997). An increase in the water–water and water–ice collision kernels caused by the turbulent/inertia mechanism is taken into account as in Pinsky and Khain (1998) and Pinsky et al. (1999, 2000). Advection of scalar values is performed using the positively defined conservative scheme proposed by Bott (1989). A detailed description of the melting process is included, following the study by Phillips et al. (2007). The computational domain is 178 km $\times$ 16 km, with resolutions of 250 and 125 m in the horizontal and vertical directions, respectively. The utilization of the

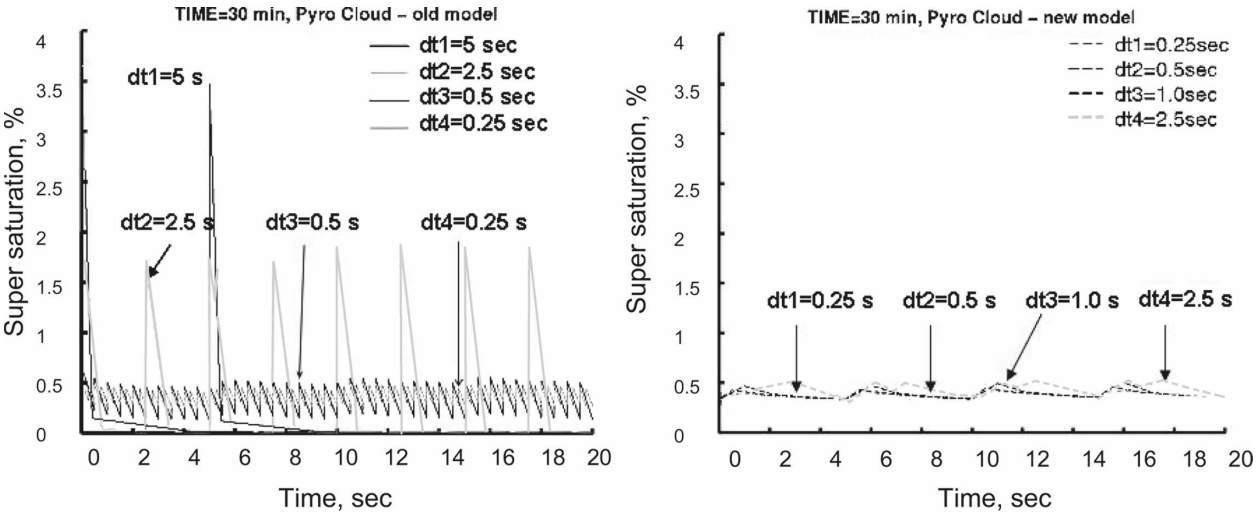

FIG. 1. Time dependence of supersaturation with respect to water S_1 using different dynamical time steps in a grid point near the cloud base of simulated pyrocloud, (left) in the old scheme and (right) in the new scheme. An increase in supersaturation takes place during the advection substep; a decrease in supersaturation is due to the diffusional growth of droplets. It is usual practice to perform droplet nucleation in the points of the supersaturation maxima.

125-m vertical resolution at all levels allows us to reproduce the cloud processes with equal and quite high accuracy at all levels. At lateral boundaries, the temperature, mixing ratio, and horizontal velocity were assumed to be equal to zero. In the upper 2-km layer, Rayleigh dumping was applied to eliminate the reflection of waves from the upper boundary.

The simulation of cloud development, especially under extremely high AP concentrations, requires an accurate description of DSD formation. The model microphysics has been updated accordingly. The main improvements are described below.

a. Calculation of supersaturation

Physical processes that take place simultaneously in nature are treated in numerical models according to a certain sequence. It is common practice in cloud models to perform the advection of all variables first and then use the supersaturation S^* obtained as a result of advection as the initial condition for droplet nucleation and diffusional growth/evaporation and ice deposition/sublimation. As a result, supersaturation is calculated using two substeps,

$$S^* = S^t + \Delta S_{\text{dyn}}, \quad \text{and} \quad S^{t+1} = S^t + \sum_i \Delta S_{i,\text{micro}}, \tag{2}$$

where ΔS_{dyn} and $\Delta S_{i,\text{micro}}$ are the changes of supersaturation during advection and after the ith microphysical time substep. The sum is taken with respect to the microphysical time substeps, which are usually shorter than the dynamical steps. In the zone of updrafts, supersaturation increases at the dynamic substep ($\Delta S_{\text{dyn}} > 0$) and decreases at microphysical substeps because of the diffusional growth of droplets and ice ($\Delta S_{i,\text{micro}} < 0$). As a result, supersaturation fluctuates at each time step. Microphysical calculations usually start with droplet and ice nucleation. In many cases, this approach leads to a reasonable droplet concentration under time steps of a few seconds. However, if the vertical velocities and/or the AP concentration are high (as in continental and pyroclouds), the utilization of a dynamical time step of a few seconds can lead to an unrealistically high S^* and to an unrealistically high concentration of nucleated droplets. An example of the time dependence of supersaturation with respect to water S_1 near the cloud base in a model-simulated pyrocloud is shown in Fig. 1 (left-hand side) for different dynamical time steps. In case of a 5-s time step, the supersaturation maximum S^* reaches 3.5%, which leads to the nucleation of more than 16 000 cm^{-3} droplets.

The appearance of supersaturation fluctuations is the result of splitting (2). In clouds, the changes of supersaturation due to advection and diffusional growth take place simultaneously, so that supersaturation does not experience fluctuations and does not reach unrealistically large magnitudes. To take this physical aspect into account, a modified method was used that combines the two steps of Eq. (2) into one. In a simplified form, this approach to the calculation of S^{t+1} can be written as

$$S^{t+1} = S^t + \Delta S_{\text{dyn}} + \sum_i \Delta S_{i,\text{micro}}, \quad (3)$$

where ΔS_{dyn} is calculated as in (2). Since the values of supersaturation are known only at two time levels (before and after advection), we assume that during the dynamical time step supersaturation changes linearly with time. So we solve the equations for supersaturation (3) under the assumption that the dynamical tendencies do not change during one dynamical time step Δt_{dyn} (see appendix A). As in the study by Khain and Sednev (1996), this solution is used for the analytical calculation of supersaturation changes during microphysical time steps, as well as for the diffusional growth of droplets and ice particles. Figure 1 (right-hand side) shows the time dependence of supersaturation in the same model grid point as in the left-hand side, but with the advection and diffusional growth treated simultaneously, that is, using approach (3). The new approach actually eliminates sharp fluctuations of supersaturation. Figure 1 shows that the results of the old approach tend to those of the new one with a decrease of Δt_{dyn}. This fact can serve as the justification of the new approach. The new method is computationally more efficient: the utilization of the 2.5-s dynamical time step in the new approach actually provides the same results as the 0.25-s time step in the earlier approach.

b. Nucleation treatment

It is usual practice in cloud models to activate APs into droplets without any change of the mixing ratio. This simplification is acceptable when the number of nucleated droplets is relatively small. The minimum droplet radius in the present model is 2 μm. In case of pyroclouds, when 4000 cm^{-3} droplets can nucleate just above the cloud base, the mass of these droplets is no longer negligible; thus, the sinking of water vapor should be taken into account to get an accurate mass budget. As is known, APs start growing when the relative humidity exceeds about 70% because of the deliquescence effect. When APs reach the cloud base, their mass is about 100 times larger than the mass of dry APs (Kogan 1991; Khain et al. 2000). As was shown by Segal and Khain (2006), the growth of APs by condensation below the cloud base (within the layer with 70%–100% relative humidity) represents the major fraction of total AP growth before their activation to droplets. The mass of water vapor that was condensed on APs within this layer is subtracted from the water vapor within the layer below the cloud base. In this way the diffusional growth of nonactivated AP is taken into account in the water vapor budget. In cases where APs penetrate the cloud through the lateral boundaries, or the activation takes place far from the cloud base (so-called in-cloud nucleation; Pinsky and Khain 2002), the mixing ratio is decreased in the points of drop nucleation, because in these cases the AP growth takes place at the expense of water vapor within clouds.

c. Numerical droplet spectrum broadening

Spectral (bin) microphysics models (SBM) face the problem of artificial DSD broadening, caused by the remapping of the DSD away from a nonregular mass grid, formed as a result of diffusional growth and collisions, onto the regular mass grid (see, e.g., Liu et al. 1995; Khain et al. 2000; Pinsky and Khain 2002). Such remapping leads to an artificial appearance on the regular grid of droplets larger than the largest droplets on the nonregular grid. The artificial formation of large droplets accelerates raindrop formation. The widely used scheme proposed by Kovetz and Olund (1969; hereafter K-O scheme) induces a significant droplet spectrum broadening (see Khain et al. 2000 for details). The K-O scheme splits the mass and concentration of hydrometeors in any bin of the nonregular mass grid between two neighboring bins of the regular grid. This procedure conserves the concentration and the mass (i.e., two moments of DSD). It is clear that the "ideal" remapping scheme (actually representing an interpolation of the size distribution onto the regular mass grid) must keep the shape of the DSD, that is, conserve all the DSD moments. The K-O scheme overestimates higher moments, which leads to an increase of the tail of the largest drops. To exclude the formation of this artificial tail, it is necessary to conserve higher DSD moments that are responsible for the flatness, skewness, and so on. A new remapping procedure conserves three moments of size distributions: the first (concentration), the third (mass), and the sixth moments (radar reflectivity; see appendix B). Figure 2 compares the DSDs calculated in the simulations of GO, S, and P clouds using the K-O scheme and the new scheme. The DSDs calculated using the new scheme are narrower and broaden with the height slower than those calculated using the K-O scheme. As shown below, the new scheme allows the reproduction of DSDs measured in situ.

3. Characteristics of simulated clouds and experimental design

The simulations of the GO, S, and P clouds have been executed under the temperature and the dewpoint vertical profiles reported by Andreae et al. (2004). According to that study, the thermodynamical conditions

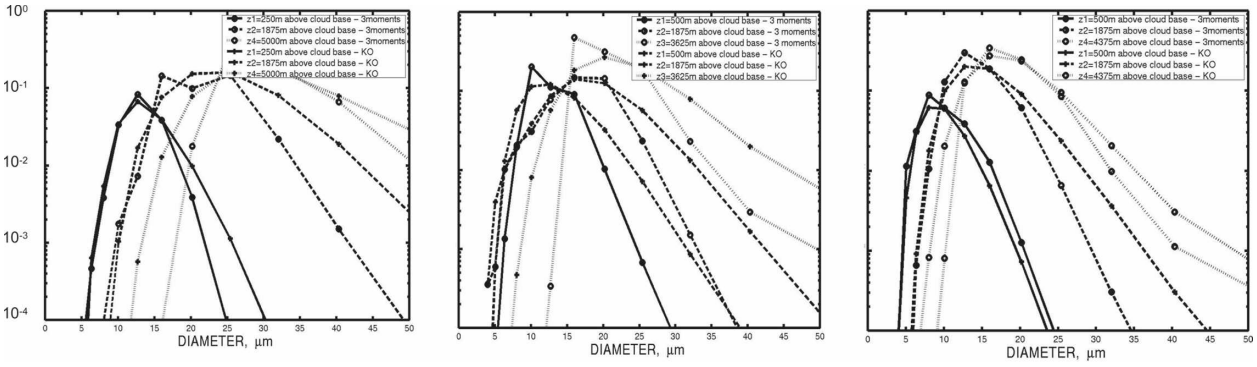

FIG. 2. DSDs calculated along the axis of (left) the simulated green-ocean cloud, (middle) the smoky cloud, and (right) the pyrocloud, using the traditional K-O scheme and a new remapping scheme. The DSDs calculated using the new scheme are narrower than those calculated using the K-O scheme. The heights are calculated above the ground.

were quite similar in all cases:[1] the surface temperature was ~34°C, and the temperature gradient was close to the dry adiabatic up to the 770-mb level and to the moist adiabatic aloft. The relative humidity (RH) was ~50% near the surface, the cloud-base level was in the vicinity of the 1.8–2-km level (770 mb, ~11.6°C), and the freezing level was located at the 4.2-km (590 mb) level. The vertical profiles of the horizontal wind were chosen using the sounding data of the nearest meteorological stations in the time periods close to those of the measurements (Fig. 3). The heat and moisture budgets in the GO and S clouds will be compared with those simulated under continental (Texas summertime; T cloud) and maritime (experiment GATE-74, 261 day; M cloud) conditions. The vertical profiles of the temperature, dewpoint, and wind speed in these cases are shown in Fig. 3 as well. The T case corresponds to a very dry (30% RH near the surface), unstable, and dirty atmosphere; the cloud-base height in this case was ~3 km (Khain and Pokrovsky 2004). The M case corresponds to a clean, wet, and comparatively stable maritime atmosphere; the RH near the surface was about 90% and the cloud-base height was 1 km (Khain et al. 2005). Thus, the clouds chosen for the analysis cover a wide range of aerosol and thermodynamic conditions: from the clean, wet, and comparatively stable M case to the extremely dry, unstable, and dirty T case. The GO and S clouds hold an intermediate position between these two extremes.

A list of numerical simulations and the corresponding parameters N_o and k is presented in Table 1. In the simulations of P clouds, the background concentration of AP was taken to be similar to that of the S cloud. There is a significant uncertainty regarding the AP concentration within a forest fire zone (Andreae et al. 2004). The main problem, however, is to reproduce the narrow DSD and its broadening with the height measured in situ. The model provides a good agreement of the droplet/AP concentration ratio with the observation data (Ramanathan et al. 2001). Owing to the uncertainty in the AP concentration, we set the AP concentration in the area of "biomass burning" (~1.4-km width and 250-m depth) to be twice as high compared with that in the surrounding areas. This value of the AP concentration allowed us to get the observed droplet concentration at the cloud base of the P clouds. In all simulations, the initial aerosol concentration was assumed constant within the 2-km-depth boundary layer, and decreased exponentially with the characteristic spatial scale of 2 km aloft. As shown by Khain and Pokrovsky (2004), the main aerosol effects on deep convective clouds come from aerosol particles penetrating the cloud base, so we do not expect a significant sensitivity of the results to the rate of the aerosol concentration decrease above the 2-km level.

To illustrate aerosol effects on the clouds developing in the dry unstable atmosphere, as well as in the more stable wet atmosphere, supplemental simulations referred to as T-m and M-c have been carried out. These simulations differ from the T and M cases in their AP concentrations (Table 1). Aerosol particles participating in droplet nucleation and serving as CCN were assumed soluble. In case of GO and S clouds, this assumption is supported by the observations (Andreae et al. 2004). It is also valid for M clouds. As regards the T

[1] In situ measurements have been carried out quite far from meteorological stations, so that the temperature and humidity profiles are not exactly known. The purpose of the study was to justify or disprove the statement that dramatic differences in cloud microphysics can be caused by aerosols, so we used temperature profiles provided by Andreae et al. (2004), which were quite similar in the GO, S, and P cloud cases.

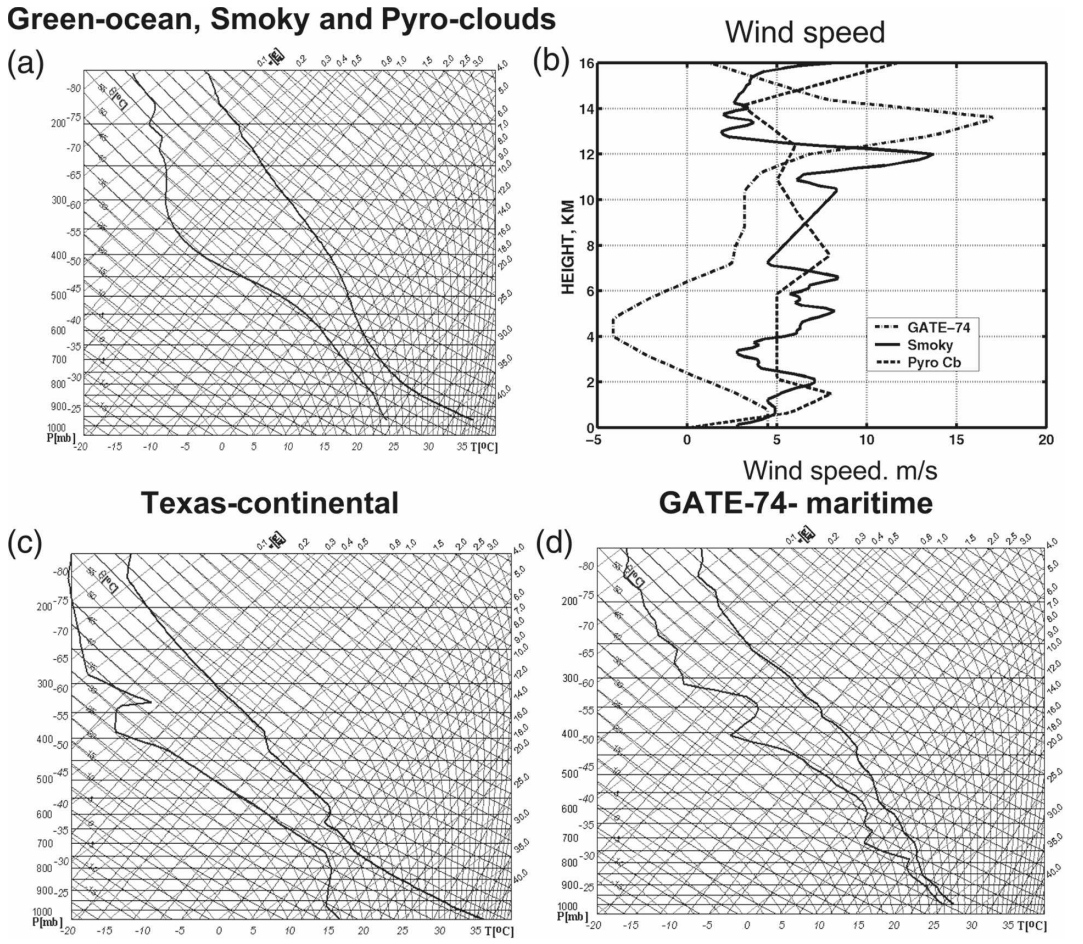

FIG. 3. (a) Vertical profiles of the temperature, dewpoint, and (b) wind velocity used in the simulations of the GO, S, and P clouds. The vertical profiles measured for (c) very continental (Texas summertime) and (d) maritime (GATE-74, 261 day) are shown as well.

cloud, some fraction of insoluble APs can be assumed. However, the insoluble aerosols do not play the role of CCN. In our study we consider only those APs that play the role of CCN. The maximum radius of dry aerosol particles in the T and S clouds was assumed equal to 1 μm, which corresponds to ~4-μm-radius nucleated droplets. In the M cloud simulation, the maximum radius of AP was set equal to 2 μm, which corresponds to ~8-μm-radius nucleated droplets. The larger size of maximum CCN in the M cloud is attributed to the formation of sea spray at the sea surface.

In all simulations, clouds were triggered by initial heating within the zone centered at $x = 54$ km. The maximum heating rate was set equal to 0.01°C s^{-1} in the center of the 4.9 km × 2 km heating area and decreased linearly to the periphery of the zones. The duration of the initial heating was 600 s in all experiments, with the exception of the P cloud simulations, where the heating was assumed to be permanent. This heating led to the formation of a 2–4 m s^{-1} vertical velocity at the cloud base, which is typical of developing convective clouds. In addition to the air heating mentioned above, the surface temperatures in the zone of the biomass burning were assumed to be high. To investigate the process of precipitation formation in the P clouds under different conditions, three sensitivity simulations (P1, P2, and P3) were performed. In the P1 run, the heating rate was set equal to 0.01°C s^{-1} and the surface temperature in the biomass burning zone was set equal to 120°C. The P2 run is similar to the P1 run, but with a wind shear similar to that used for the S cloud simulation and a 170°C surface temperature in the zone of the biomass burning. To simulate a more intense and rapidly developing P cloud, the P3 run was performed, which differs from the P1 run in the heating rate, which was 0.075°C s^{-1}, as well as in the 170°C surface temperature. The propagation speed of the fire was assumed to be zero, which is similar to the assumption

TABLE 1. The list of simulations and parameters characterizing aerosol distributions.

Type of cloud	Short title	N_0 (cm^{-3})	k	References
Green-ocean clouds	GO clouds	100 cm^{-3} 400 cm^{-3}	0.92	Andreae et al. (2004); Roberts et al. (2002); Rissler et al. (2004)
Smoky clouds	S clouds	6880 cm^{-3}	0.718	The same
Pyroclouds	P clouds, subdivided as P1, P2, P3 clouds	6880 cm^{-3} in environment, 13 760 cm^{-3} within the forest fire zone	0.718	Eagan et al. (1974); Andreae et al. (2004); Roberts et al. (2002); Rissler et al. (2004) 13 760 cm^{-3} was chosen to capture the droplet concentration observed at the cloud base
Texas continental clouds with high CCN concentration	T clouds	2500 cm^{-3}	0.308	Rosenfeld and Woodley (2000) Khain et al. (2001b, 2004, 2005); Khain and Pokrovsky (2004)
Texas sounding, low aerosol concentration	T-m clouds	100 cm^{-3}	0.921	Sensitivity study
GATE-74 deep maritime cloud	M clouds	100 cm^{-3}	0.921	Khain et al. (2001b, 2004, 2005)
Maritime sounding, but high CCN concentration	M-c clouds	2500 cm^{-3} 100 cm^{-3}	0.308 0.921	Sensitivity study; CCN distribution was represented as a sum of continental and maritime distributions
Maritime clouds, but with lower* relative humidity	M-80 clouds	100 cm^{-3}	0.921	Sensitivity experiment
Maritime clouds, but with lower relative humidity and high aerosol concentration	M-c-80 clouds	2500 cm^{-3} 100 cm^{-3}	0.308 0.92	Sensitivity study; CCN distribution was represented as a sum of continental and maritime distributions

* In M-80, relative humidity was 10% lower over the whole atmosphere as compared with GATE-74 conditions, so the RH at the surface was 80% instead of 90%.

that the propagation speed was significantly slower than the wind speed in the middle atmosphere.

The surface temperature and the water vapor mixing ratio were assumed unchangeable during the simulations. The maximum value of the dynamical time step was 5 s. Most simulations were conducted for 3–4 h. This time period was longer than the lifetime of all clouds except the pyroclouds.

4. Results: Microphysical structure of the green-ocean and smoky clouds

Because the conditions of the GO and S clouds simulations differ only in the AP concentrations, the differences between their microphysical and dynamical structures can be attributed to the aerosol effect only. Because the DSD shape determines the microphysical structure and the precipitation at all stages of the cloud evolution, an adequate representation of the DSD shape and its evolution with height is the necessary condition determining the reliability of all other results. Figure 4 shows the DSDs at different distances above the cloud base in the growing GO, S, and P clouds, calculated and measured in situ. Within the first few kilometers above the cloud base, the DSDs in all P cloud simulations were quite similar. All DSDs were calculated by averaging the DSDs in the horizontal direction over the cloud updraft zones. Such averaging corresponds to the calculation procedure of the DSD measured in situ. One can see that the model reproduces well the observed DSDs within 2 km above the cloud base, where the observations were available. At 1.5–2 km above the cloud base, the mean volume diameters were about 25, 15, and 12 μm in the GO, S, and P clouds, respectively. In the S and P clouds the DSD width increases with the height much more slowly than in the GO clouds, indicating a significant difference in the drop diffusion and collision rates in these cases.

Figure 5 shows the fields of droplet concentration, the cloud water content (CWC), and the rainwater content (RWC) in the GO (N_o = 400 cm^{-3}) and S clouds at t = 25–30 min. The droplet concentration in the S clouds (with a maximum of 2000 cm^{-3}) is in good agreement with the concentration measured in situ (2000–2200 cm^{-3}). As mentioned by Andreae et al. (2004), the droplet concentration for the GO cloud reported in their paper (~1000 cm^{-3}) had been significantly overestimated (it exceeded the CN concentra-

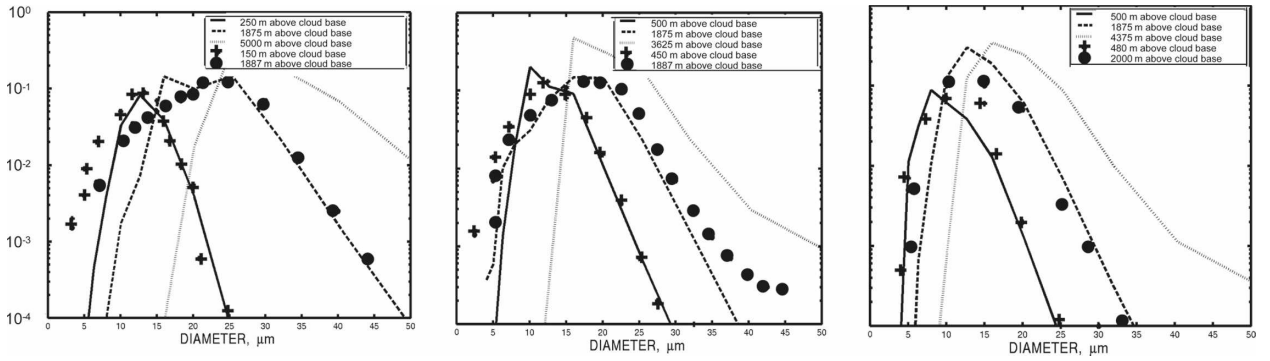

FIG. 4. DSDs at different distances above the cloud base of (left) the growing green-ocean cloud, (middle) the smoky cloud, and (right) the pyrocloud, simulated and measured in situ. The calculated DSD are denoted by lines; dots and pluses represent the measurements. The measured DSDs are plotted according to Andreae et al. (2004). There were no DSD measurements above 4200 m, i.e., ~2.2 km above cloud base.

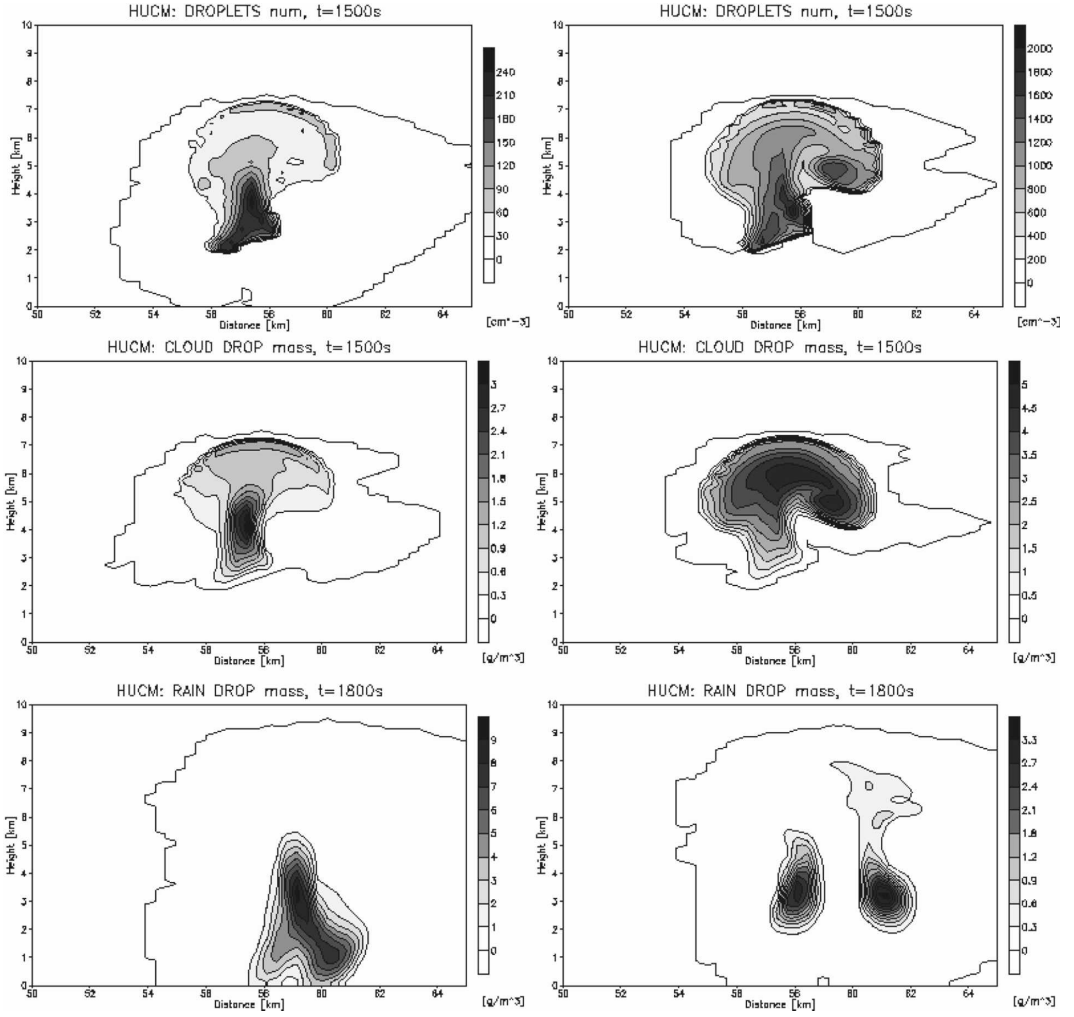

FIG. 5. Fields of droplet concentration, CWC, and RWC in (left) the green-ocean and (right) the smoky clouds at t = 25–30 min.

tion). In the simulations, the droplet concentration maximum is about 250 cm^{-3}, which seems to be a reasonable value. The CWC maximum in the GO cloud (3.0 gm^{-3}) is significantly smaller than that in the S cloud (5 gm^{-3}), which can be attributed to the rapid raindrop formation in the former case. Raindrop formation in the GO cloud takes place at ~1.5 km above the cloud base, which agrees well with the observations. The contribution of warm rain to total rain is dominant in this case. In the S cloud, raindrops form at ~4–5 km above the cloud base and fall in the zone of downdrafts. The raindrops fully evaporate within the dry air and do not reach the surface.

The difference in the warm microstructure of the clouds determines the difference in their ice microstructure and the precipitation type. Figure 6 shows that the total ice content in the S cloud is much larger than that in the GO cloud. The maximum values of crystal, graupel, hail, and snow mass content in the GO cloud are, 0.27, 2.5, 0.3, and 0.05 g m^{-3}, respectively. These contents in the S cloud were 0.5, 4, 2.7, and 0.65 g m^{-3}, respectively. The GO cloud does not actually produce hail because of the lack of a significant amount of supercooled water above the 5-km level (Fig. 5) required to rime graupel to hail. Most raindrops in the GO cloud form below or slightly above the freezing level—that is, precipitation is mainly warm rain. The ice mass content is relatively small in the GO clouds. This feature is even more pronounced in maritime (blue ocean) convection. In the S and P clouds, supercooled drops reach sizes exceeding ~50–100 μm at heights above 5 km. Most of these raindrops efficiently collide with ice crystals caused by the primary ice nucleation and give rise to graupel and hail formation. The significant content of supercooled water in the S cloud determines the significant riming rate of ice crystals to graupel and graupel to hail. Most graupel forms above the 6-km level in the S clouds and above the 7.5-km level in the P clouds, which indicates a good quantitative agreement with the values reported by Andreae et al. (2004). A significant fraction of supercooled droplets remains small (below 20 μm in radius). These droplets reach a homogeneous freezing level and give rise to the formation of ice crystal concentrations as high as a few hundred per cubic centimeter, similar to that observed in continental summertime Texas clouds (Rosenfeld and Woodley 2000). Collisions of ice crystals determine intense snow (aggregate) formation. Efficient riming transfers snow into graupel, so that the snow mass content is lower than that of graupel and hail at $t = 40$ min (Fig. 6). The mass content of hail in the S cloud at 40 min is smaller than that of graupel. Having the largest fall velocity, hail penetrates into the layer with positive temperatures by about 2 km. Figure 6 also shows that the S cloud has a higher cloud top than the GO cloud.

Figure 7 (top) shows the size distributions of graupel in the GO cloud and the S cloud at different heights at 40 min in the points shown by white circles in Fig. 6. Graupel size distributions are wide, with diameter ranging from 50 μm to 0.9 cm. Note that the maximum size of graupel, hail, and snow is limited in the model by the choice of the mass grid containing 33 mass bins. The analysis of large graupel and hailstone formation will be performed in a separate study where 43 bins are used. The mass of graupel in the S cloud is larger, but graupel reaches larger sizes in the GO cloud. The latter can be attributed to the fact that in the GO cloud graupel forms from the freezing (heterogeneously or in collision with crystals) of large raindrops. The width of graupel size distributions is maximum at ~6 km. Above this level, droplets are smaller and riming results in the formation of graupel of a smaller size. Figure 8 shows the fields of graupel and snow mass contents in the GO and the S clouds at the decaying cloud stage ($t = 4800$ s). While at this stage the GO cloud ice hydrometeors consist mainly of graupel, in the S cloud snow (aggregate) contributes significantly to the ice mass and precipitation. A smaller mass of snow in the GO cloud can be attributed to the fact that drops in the GO cloud are as a rule larger than those in the S cloud. According to the rules used in the model, the collision of a drop and an ice crystal/aggregate produces either graupel, if the mass of the drop is larger, or crystal/aggregate, if the mass of the latter is larger (see Khain et al. 2004). Therefore, water–ice crystal collisions in the GO cloud lead mainly to graupel formation.

5. Results: Microphysical structure of pyroclouds

The early development stage of the P clouds (first 10 min) resembles that of the S cloud. However, because of a higher vertical velocity (~10 m s^{-1} at the cloud base instead of 3–4 m s^{-1} in the S cloud) and a higher AP concentration, the droplet concentration reaches 2400–2700 cm^{-3}, in agreement with the observations (Andreae et al. 2004).

Three P cloud simulations (P1–P3) were performed to investigate the sensitivity of the structure and precipitation formation in P clouds to surface heating. Precipitation formation in these simulations turned out quite different. In the P1 and the P2 runs, which both have a relatively weak heating rate, precipitation starts later than in the S cloud, but in the P3 run with a higher heating rate, precipitation begins earlier than in the S cloud and increases with time faster than in all other cases. In all simulations, precipitation from the P clouds

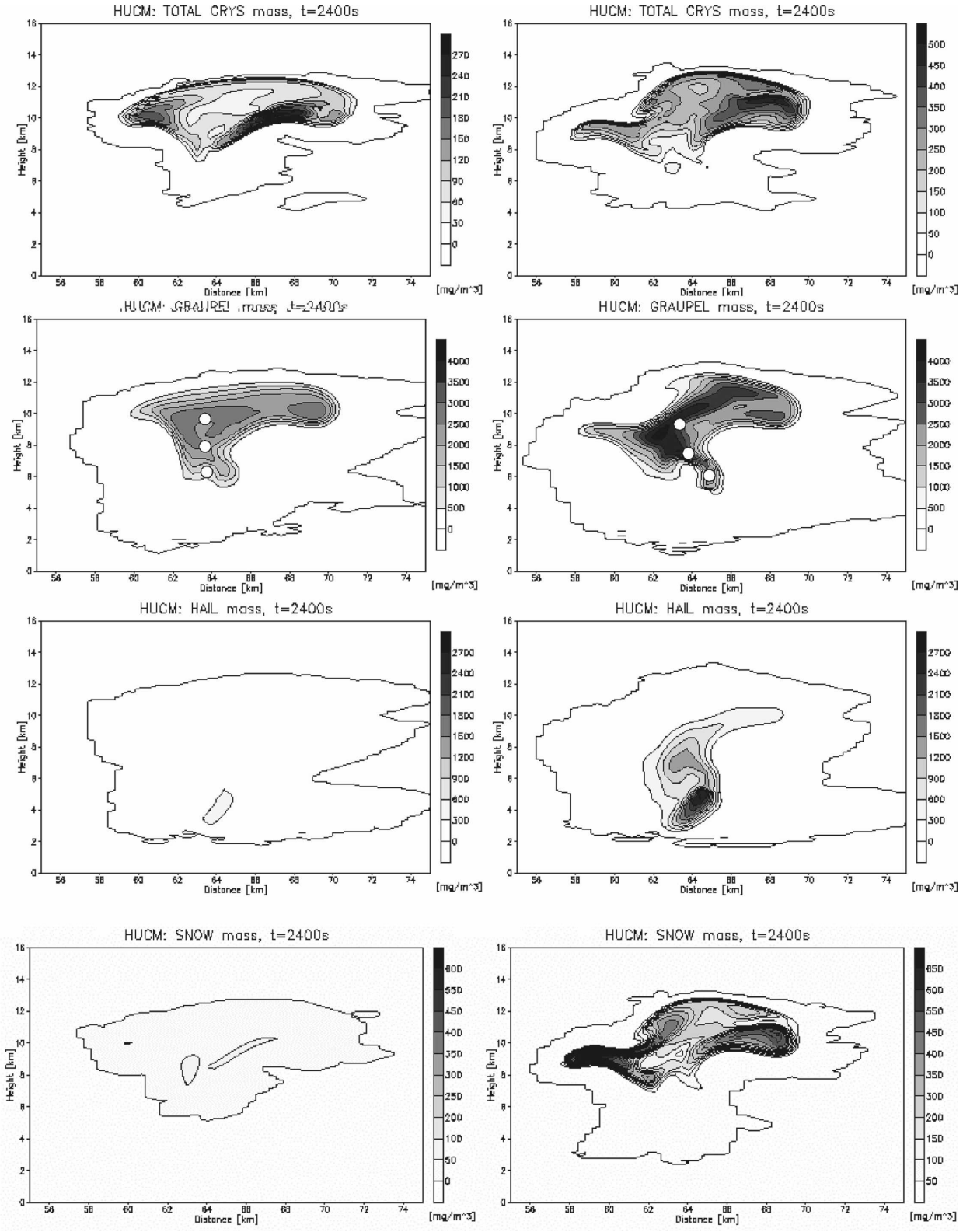

FIG. 6. Fields of mass contents of ice crystals, graupel, hail, and snow in (left) the green-ocean and (right) the smoky cloud at t = 40 min.

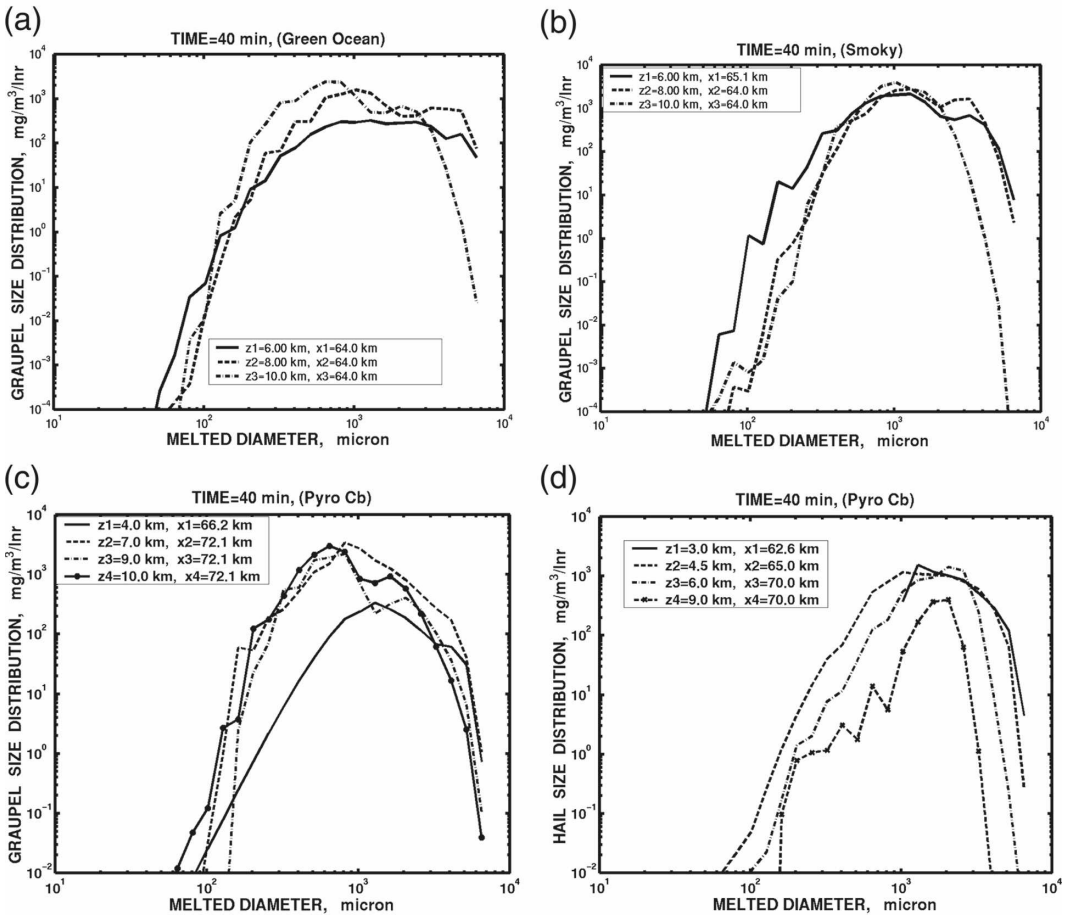

FIG. 7. Mass distributions of graupel in the (a) GO, (b) S, and (c) P cloud at different heights at 40 min. (d) The size distributions of hail in the pyrocloud obtained in the simulation P3 (see the text) are also shown. The size distributions are plotted in the points marked by white circles shown in Figs. 6 and 10.

exceeds that from other types of clouds after 60–80 min (see below). These features of the model P clouds are related to the following factors. First, the location of cloud formation is controlled by the location of the biomass burning zone. The wind shear tilts the cloud axis and breaks the cloud into several periodically changing zones of updrafts and downdrafts with the amplitude decaying downwind (Fig. 9). Second, the maximum vertical velocities in the P cloud are higher (up to 25–35 m s^{-1}) than those in the GO and S clouds (10–15 m s^{-1}). Third, the high horizontal temperature gradient in the boundary layer leads to the formation of a strong vortex (updraft–downdraft pair) downwind of the cloud updraft.

Figure 9 shows the fields of vertical velocity, droplet concentration, CWC, and RWC in the P1 simulation at 2100 s. One can see the formation of several clouds: the primary cloud forms above the area of the biomass burning and the secondary cloud forms 7 km downwind in the updrafts caused by the wavelike structure (the gravity wave) of the vertical velocity field. The primary cloud with a droplet concentration of 2400–3000 cm^{-3} and LWC maximum of 4.5 g m^{-3} does not precipitate. The AP concentration and the vertical velocity at the cloud base of the secondary cloud are smaller, resulting in a lower droplet concentration. As a result, precipitation starts falling from the secondary cloud located at a significant distance from the primary one. Precipitation at a later stage of the P cloud evolution consists of melted ice particles. Precipitation formation in the P2 run took place similarly to that in P1 (not shown).

Precipitation onset in the P3 cloud differs from that in the P1 and P2 runs. A stronger heating leads to a higher vertical velocity so the P3 cloud reaches a height of 10–12 km in 15 min. The early beginning of precipitation on the surface (~20 min) is caused by graupel descending within the region of strong downdrafts. The formation of the downdrafts follows from the continu-

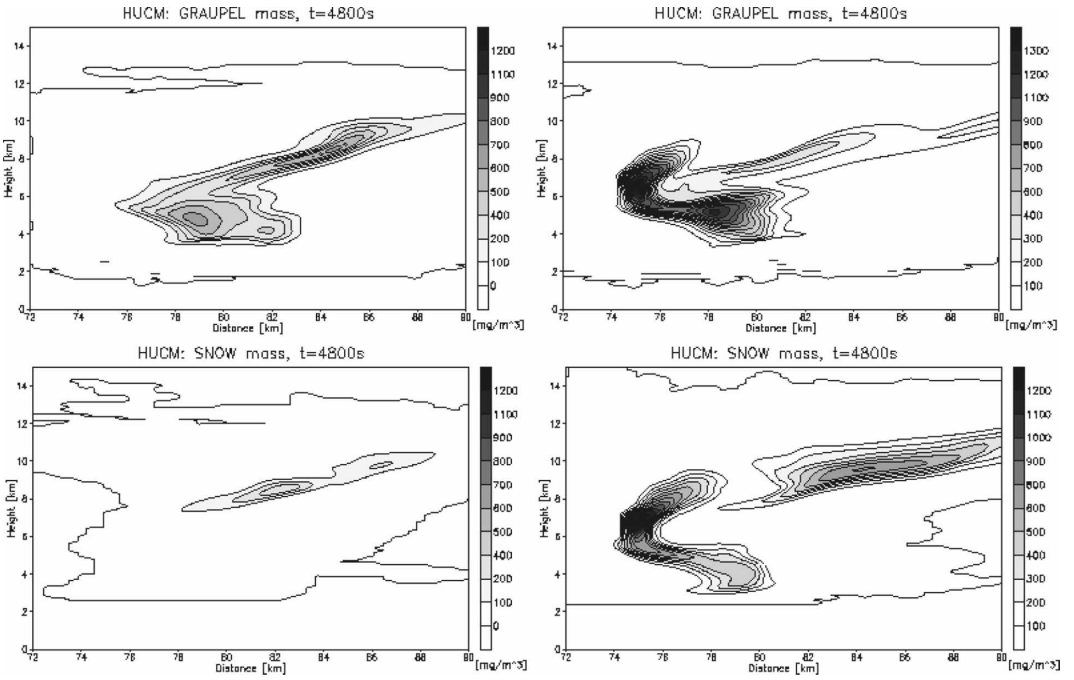

FIG. 8. Fields of the graupel and snow mass contents in the (left) GO and (right) S clouds at the decaying stage of the cloud evolution (t = 4800 s).

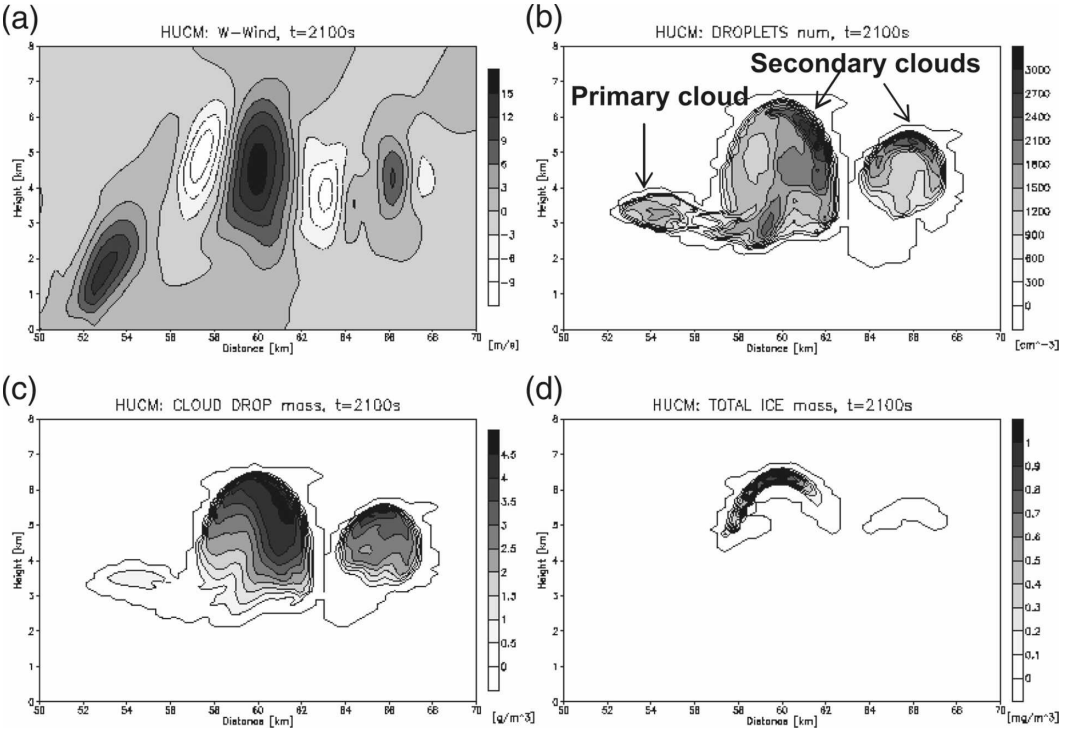

FIG. 9. Fields of the (a) vertical velocity, (b) the droplet concentration, (c) CWC, and (d) the total ice in the pyrocloud simulation P1 at 2100 s. Raindrops form in the secondary cloud located about 7 km downwind of the primary one.

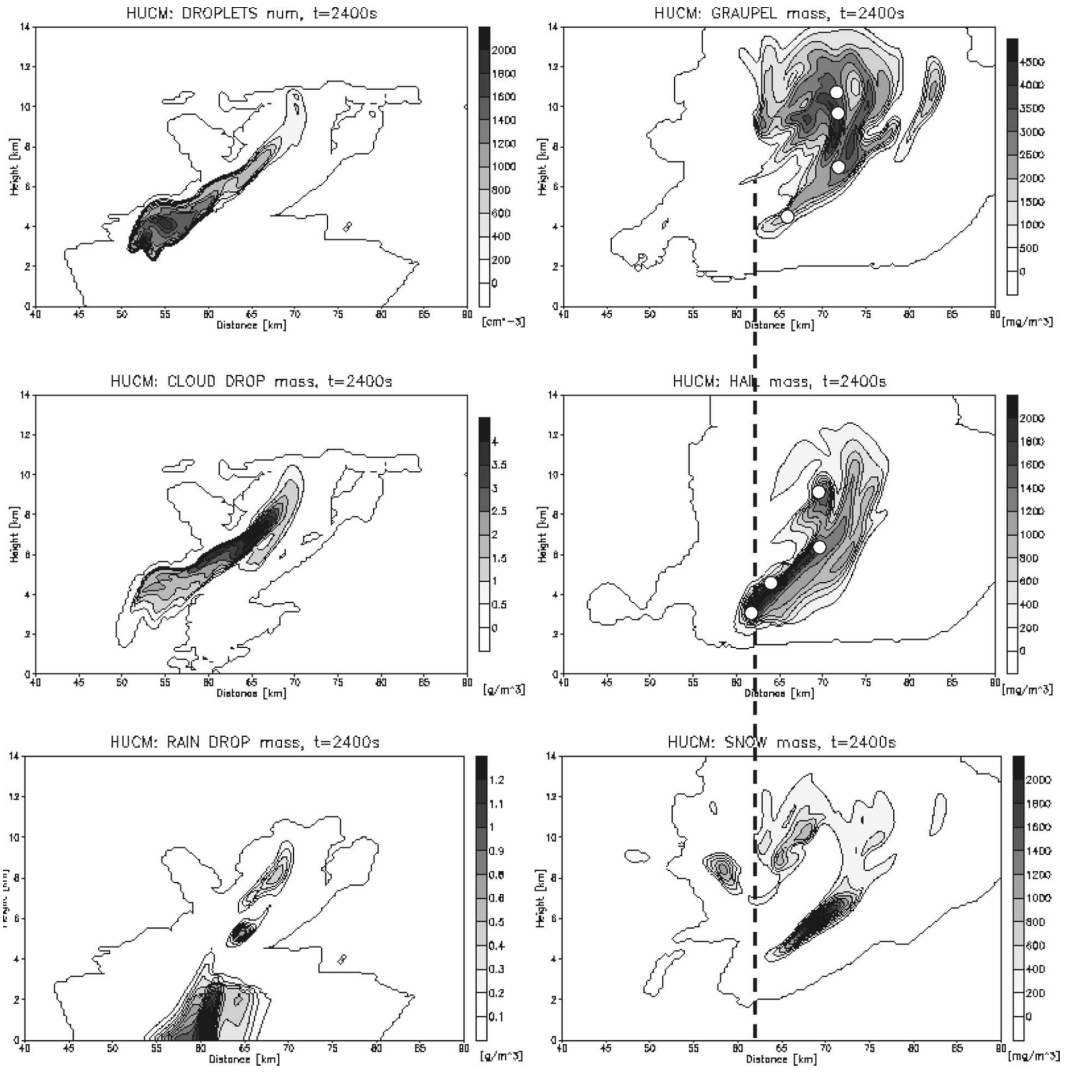

FIG. 10. (left) Fields of drop concentration, CWC, and RWC and (right) fields of graupel, hail, and snow mass contents in pyrocloud (P-3) at $t = 40$ min. Dashed line shows the location of the maximum rain content below 3 km. White points in the panels of graupel and hail content fields show the points in the cloud for which size distributions are plotted in Fig. 7.

ity equation. Updrafts change the pressure field in such a way as to create compensating downdrafts. The "compensating" downdrafts are increased by the condensate loading, as well as by the cooling caused by the sublimation of ice, the evaporation of droplets, and melting.

The microphysical structure of the P3 cloud at 40 min is illustrated in Figs. 7 and 10. The significant difference between the ice microstructure of the model P and S clouds is caused mainly by the difference between their dynamics. The high vertical velocities in the P cloud transport small cloud droplets to upper levels. As a result, the region of graupel formation coincides with the zone of high LWC. Since the droplets are small, graupel particles are smaller than those in the GO and S clouds; however, their concentration is higher (Fig. 7). The large LWC fosters the graupel growth and hail formation by riming of graupel as described in section 2. One can see a significant increase in the hail size in the zone below 5 km (Fig. 10). At $z = 3$ km, there is no hail smaller than 1000 μm because of small hail melting. Ice particles tend to fall within strong downdrafts. Large hail penetrates over 2.5 km into the layer of warm temperature. As soon as the first ice particles reach the boundary layer downwind of the cloud updrafts, a new efficient rain formation mechanism arises. This mechanism is related to the hydrometeor recirculation illustrated in Fig. 11. The high-temperature horizontal contrast near the surface leads to the formation

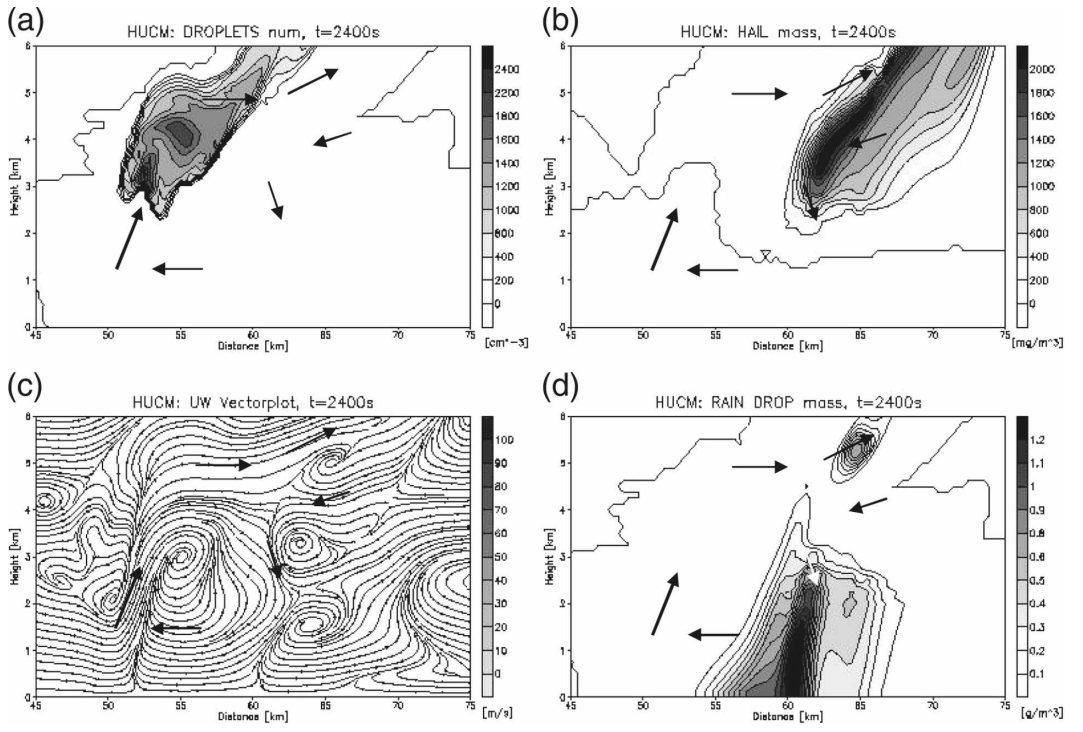

FIG. 11. Fields of (a) the droplet concentration, (b) hail mass content, (c) streamfunction, and (d) RWC in the P-3 cloud. The arrows indicate air circulation leading to the recirculation of hydrometeors, when precipitating particles falling outside the cloud are involved with cloud updraft and foster rapid precipitation formation even under very high aerosol concentration.

of a mighty vortex within the lower 4-km layer, so that the horizontal velocity in the subcloud layer is directed toward the cloud updraft. While the largest drops formed by melting are falling, smaller raindrops penetrate into the cloud. As a result, newly nucleated cloud droplets coexist with much larger drops just above the cloud base to the right of the cloud axis. The droplet mass distributions to the right of the cloud axis indicate the existence of intensive collisions and raindrop formation at heights as low as 4–5 km. These raindrops partially freeze above the freezing level (4.1 km), leading to the formation of hail and graupel at comparatively low (5 km) levels, and then fall down (Fig. 11). Figure 7 shows that hail size distribution at $z = 3.5$–4.5 km is much wider and corresponds to a much higher hail mass content than at the higher levels. As a result of this recirculation, hail and graupel precipitation forms in the extremely polluted atmosphere. Melting leads to air cooling, which accelerates the recirculation. Thus, because of the process of recirculation, the extremely high droplet concentration in P clouds can coexist with intense precipitation. At a later stage all ice hydrometeors (graupel, hail, and snow) contribute significantly to the melted precipitation.

One can see that pyroclouds represent complicated structures that can contain several clouds. The onset of precipitation can be either caused by strong downdrafts downwind of the primary cloud or generated in secondary clouds located tens of kilometers downwind from the nonprecipitating primary cloud. In this case, the primary cloud does not precipitate. This result can create a delusive impression that pyroclouds do not precipitate.

6. Analysis of aerosol effects on precipitation and precipitation efficiency

a. Time dependence of precipitation and precipitation efficiency

We will characterize aerosol effects on the precipitation by two parameters: by the accumulated rain amount and by the precipitation efficiency (PE). If toward the end of a simulation a cloud (or a cloud system) disappears, the accumulated precipitation at the surface is equal to the difference between the hydrometeor condensate mass formed by the drop condensation and ice deposition (termed G for generation) and the precipitation loss due to evaporation and ice sublimation L, that is,

$$P = G - L. \tag{4}$$

Note that the condensate generation G leads to drying and heating, while the loss L leads to the moistening and cooling of the troposphere. The net precipitation means the net heating and drying effects of precipitating clouds. Aerosols affect both items of the moisture budget (4). Respectively, the change in precipitation ΔP induced by aerosols can be written as

$$\Delta P = \Delta G - \Delta L, \tag{5}$$

where ΔG and ΔL are aerosol-induced changes in the generation and the loss of hydrometeor mass, respectively. Note that usually $\Delta G \ll G$, and $\Delta L \ll L$. Besides, ΔG and ΔL are often of the same order of magnitude (see below). Hence, the aerosol-induced precipitation change ΔP can be two orders of magnitude less than either G or L, which indicates the necessity of a high precision of the model representation of each item of water and heat budgets (see examples in LiTa).

There are several definitions of the precipitation efficiency PE (e.g., Hobbs et al. 1980; Ferrier et al. 1996; Wang 2005; Sui et al. 2007). We apply here the definition used by Khain (2006), which follows from the condensate mass budget considerations and has a clear physical meaning:

$$\mathrm{PE} = \frac{P}{G}. \tag{6}$$

In spite of the fact that it is difficult to extract the PE values from observations, the comparison of the PE values obtained in different simulations (and in some observational studies) provides important information about the physics of aerosol effects on precipitation. In case a cloud or a cloud system disappears toward the end of a simulation, PE is calculated as the ratio of accumulated rain to the accumulated condensate, which characterizes the integral response of the system to aerosols. The PE can be also regarded as a function of time—PE(t), where $P(t)$ and $G(t)$ are the time-averaged rain rate and the generation rate—which is close to the definition of PE used by Hobbs et al. (1980). The changes of PE induced by different factors, including the aerosol effect, can be written as

$$\Delta\mathrm{PE} = \frac{\Delta P}{G} - \mathrm{PE}\,\frac{\Delta G}{G}, \tag{7}$$

or, in a more convenient form, as

$$\frac{\Delta\mathrm{PE}}{\mathrm{PE}} = \frac{\Delta P}{P} - \frac{\Delta G}{G}. \tag{8}$$

Figure 12 shows the time dependence of the accumulated rain amount in two GO cloud simulations (with N_o = 400 cm^{-3} and 100 cm^{-3}), in three P cloud simulations, and in the maritime GATE-74 and summertime continental Texas clouds. One can see that precipitation from the S cloud begins with a 12-min delay as compared with that from the M cloud, and with a 6-min delay as compared with the GO clouds. The net accumulated rain amount from a single GO cloud exceeds that from the S cloud by about 15%. A sharp increase in the accumulated rain in the GO clouds at 30–35 min is caused by the warm rain. The low slope of the curves at $t > 35$ min is related to melted precipitation, which is only a small contribution to the total precipitation in the GO simulations. On the contrary, precipitation from the S cloud is determined by melted rain of smaller intensity but of a longer duration (up to ~100 min). The accumulated precipitation is the largest in the M cloud and the smallest in the continental T cloud. These features are the consequence of the microphysical structure of the GO and S clouds discussed above. The plateaus toward 2–3 h indicate a decay of convection. This fact simplifies the analysis of the aerosol effects on the budget of the corresponding clouds. The accumulated rain in the P clouds increases with time because of the continuous heating from the surface.

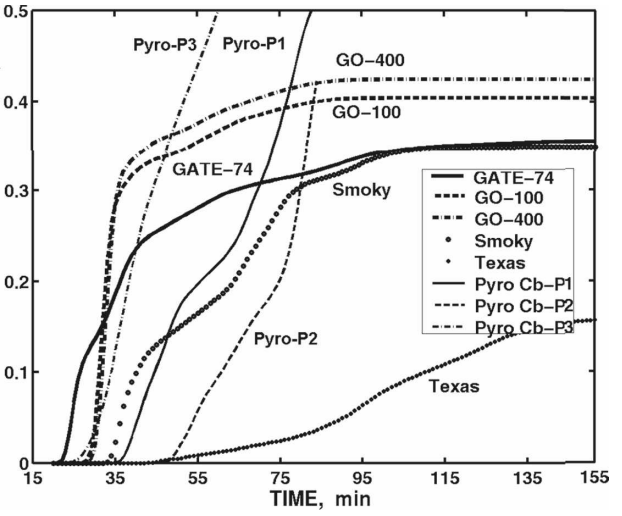

FIG. 12. Time dependence of the accumulated rain amount in all simulations including two GO simulations with No = 400 cm^{-3} and 100 cm^{-3}, three simulations of the P cloud, the maritime GATE-74, smoky, and summertime continental Texas clouds.

Figure 13 shows the time dependence of accumulated rain in the simulations M, M-c, M80, M-c-80, T, and T-m. A mere 10% decrease in RH led to a dramatic decrease in precipitation in M-80 and to the inversion of the precipitation response to aerosols: while the precipitation in M-c was larger than in the M clouds, the precipitation in M-c-80 is smaller than that in the M-80 cloud. The reasons for this difference will be discussed

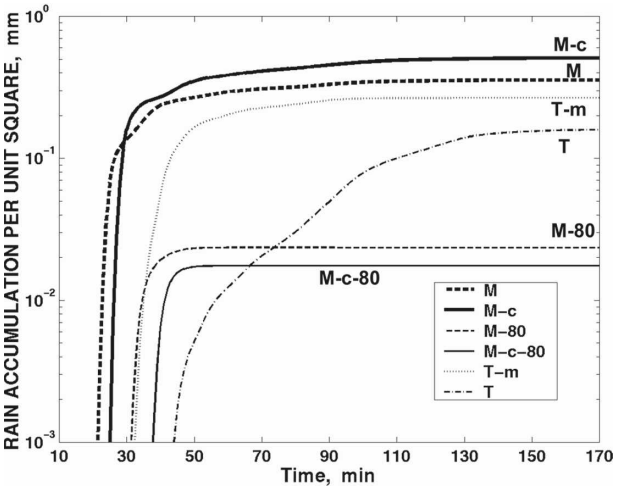

FIG. 13. Time dependence of the accumulated rain in the simulations M and M-c, M-80 and M-c-80, and T and T-m. A decrease in RH of only 10% led to a dramatic decrease in precipitation in the M-80 and to the inversion of precipitation response to aerosols: while the precipitation in the M-c was larger than in the M clouds, the precipitation in the M-c-80 is smaller than that in the M cloud.

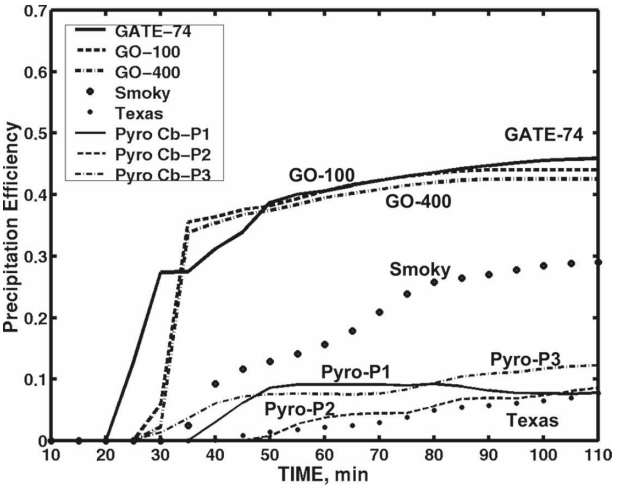

FIG. 14. Time dependence of the precipitation efficiency in different simulations.

below in the analysis of the heat and moisture budgets.

Figure 14 shows the time dependence of the precipitation efficiency in most simulations. The PE of smoky clouds is 2–3 times smaller than that of the clouds arising in clean air. The PE of tropical M clouds is 4–5 times higher than that of T clouds. These results agree well with the evaluations of PE presented by Braham (1952), Marwitz (1972), Heymsfield and Schotz (1985), and Li et al. (2002). The higher PE in M clouds can be attributed to a small precipitation loss under high relative humidity.

The PE of the P clouds remains small in spite of permanent precipitation. The physical reason for the decrease in the precipitation efficiency of the clouds developing in polluted air is that the larger generation of the hydrometeor mass is accompanied by even a larger loss of precipitating mass by sublimation and evaporation. The latter will be demonstrated in detail using the heat and moisture budgets.

b. The mass, heat, and moisture budgets

Figure 15 compares the water, ice, and total mass contents in the computational area in the M and M-c, T and T-m, T and M, and S and GO simulations, respectively. These quantities characterize the generation item in the mass budget. In the dry unstable atmosphere of the T case, the total hydrometeor mass is larger than in all other cases in spite of the fact that precipitation in this case in minimum. One can see that the hydrometeor mass in polluted clouds is higher than that in the clouds developing in clean air. This excess in dirty clouds depends on thermodynamic conditions (including instability). The largest difference takes place between the T and M clouds, where the difference in the AP concentration is accompanied by a significant difference in the instability. Note that in spite of a larger production of condensate, precipitation in the T cloud is several times smaller than in the M cloud. It is of great importance that we consider clouds with a high (~4 km) freezing level above the ground. Raindrops in clouds developing in clean air form mostly below the 4-km level and fall, leaving a relatively small hydrometeor mass in the air aloft. In contrast, most drops in the clouds developing in dirty (and/or more unstable) air ascend above the freezing level and produce ice growing by deposition. Thus, the difference in the aerosol concentration leads to a significant difference in the cloud microphysics of such clouds. Figure 15 shows that the difference in the mass contents is mainly due to the difference in the ice contents. Even if the soundings are similar, the liquid water content in polluted clouds is larger as well. This difference means that the formation of clouds in polluted air should be accompanied by a larger latent heat release (larger heating). Figure 15 also shows that the lifetime of clouds arising in polluted atmospheres is longer, which can be attributed to the existence of a large quantity of ice crystals and small graupel with a long residential time.

Figure 16 shows the vertical profiles of horizontally averaged (per one grid of the computational area) heating/cooling and drying/moistening for a 4-h period in pairings of simulations with similar thermodynamics but different aerosol concentrations: the GO and S

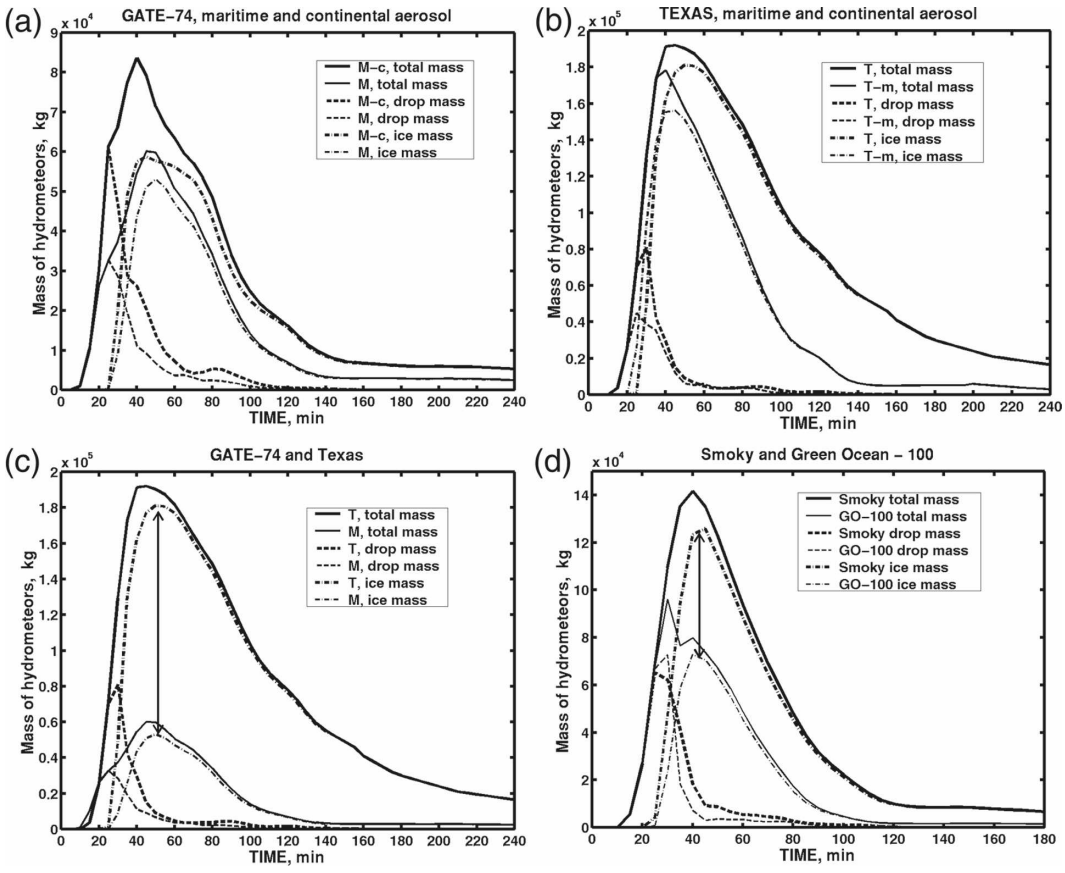

FIG. 15. Time dependencies of the water content, the total ice content, and the total hydrometeor content in the computational area in the simulations: (a) the maritime sounding, low (M) and high AP concentration (M-c), (b) the continental sounding, high (T) and low aerosol concentration (T-m), (c) the maritime cloud (M) and the continental cloud typical of Texas, and (d) the S and GO clouds. The arrows show the differences between the maximum of the total ice contents in two latter cases.

clouds and then the M and M-c clouds. The heat and moisture budgets in the T and T-m cases (not shown) are similar to those of the S–GO pair. The heating–cooling and moistening–drying differences representing, respectively, the net convective heating and the net convective moistening are shown as well. The areas between the net heating and net moistening profiles represent the measure of aerosol effects on precipitation. The aerosol-induced net drying and heating of the atmosphere indicates the increase in precipitation, while the net moistening and cooling indicates the decrease in precipitation. Note that the areas between the profiles depicting the net effect (i.e., aerosol effects on precipitation) are much smaller than those formed by the curves depicting heating (cooling) or drying (moistening), as shown above. The latter imposes heavy demands on the precision of the calculation of different items of the budgets to reveal the aerosol effects on precipitation. Several important conclusions follow from the analysis of Fig. 16:

(i) An increase in the aerosol concentration leads to an increase in both the generation G, as can be seen in Fig. 15, and the loss L of the hydrometeor mass, that is, $\Delta G > 0$ and $\Delta L > 0$. The increase in the condensate generation with the aerosol concentration can be attributed to a longer residential time of drops and ice within clouds, when the aerosol concentration is high. The increase in the aerosol concentration leads to an extra condensational growth of droplets and depositional growth of ice. Further, the release of latent heat of freezing is higher in dirty clouds because of more efficient ice processes. The increase in the condensate loss with the aerosol concentration can be attributed to the fact that in dirty clouds particles fall from higher levels, often far from the cloud updrafts (i.e., in dry air). This result had been obtained and discussed earlier by Khain et al. (2005).

(ii) In the M and M-c simulations the atmosphere is quite wet, so an increase in the aerosol concentra-

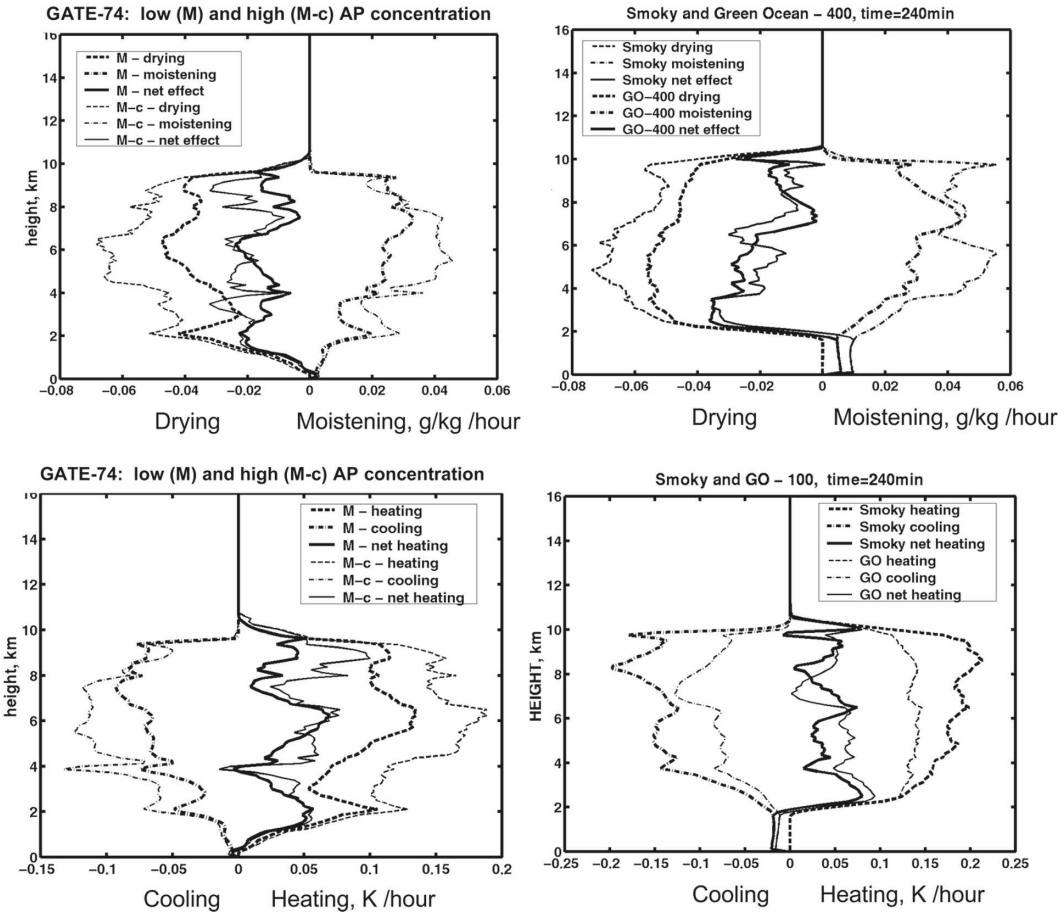

FIG. 16. The vertical profiles of horizontally averaged (top) moistening/drying and (bottom) heating/cooling (per one grid of the computational area) and over the 4-h period in the simulations for (left) the simulations M and M-c clouds and (right) the GO and S clouds. The differences between moistening and drying, as well as between heating and cooling, represent the net effects, which are shown as well (solid lines). The M-c cloud heats and dries the atmosphere to a larger degree than the M cloud, i.e., the precipitation from the tropical maritime deep clouds increases in dirty air. In contrast, the precipitation from continental clouds developing in a comparatively dry atmosphere increases in clean air.

tion increases the condensate production to a higher degree than the loss ($\Delta G > \Delta L$). As a result, the M-c cloud heats and moistens the atmosphere to a larger degree than the M cloud, that is, the precipitation from the tropical deep maritime clouds increases in dirty air.

(iii) In the GO simulations (as well as in the Texas case) the atmosphere is quite dry, so an increase in the aerosol concentration increases the condensate loss to a higher degree than its production ($\Delta L > \Delta G$). As a result, the S and T clouds (not shown) heat and moisten the atmosphere to a smaller degree than the GO and T-m clouds, that is, the precipitation from continental clouds developing in a comparatively dry atmosphere decreases in dirty air.

(iv) It follows from (8), since $\Delta G > 0$, that an increase in the aerosol concentration decreases the precipitation efficiency to a relatively higher degree than the accumulated precipitation. The latter explains the significant difference in the PE between the clean-air and the polluted-air clouds, as well as the very low PE of pyroclouds in spite of intense precipitation.

7. Classification of aerosol effects on precipitation

The results of simulations and budget considerations allow us to propose a scheme that could be useful for the classification of aerosol effects on precipitation (Fig. 17). Let us consider an initial situation characterized, say, by a relatively small aerosol concentration. This initial situation is schematically denoted by point

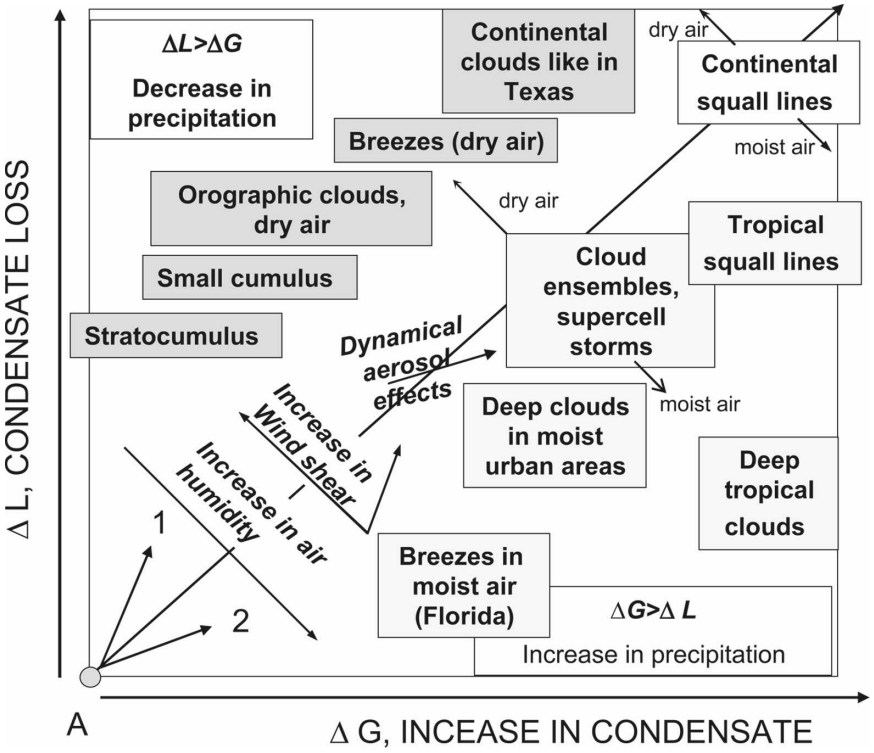

FIG. 17. A schematic diagram of the aerosol effects on clouds and cloud systems of different types. The zone above the diagonal corresponds to a decrease in precipitation with the aerosol concentration. The zone below the diagonal corresponds to an increase in precipitation with the increase in the AP concentration.

A. An increase in the aerosol concentration leads, as shown above, to an increase in both the condensate production and the condensate loss. The diagonal line in Fig. 17 separates two zones. The upper zone corresponds to the condition $\Delta L > \Delta G$, in which the precipitation decreases (scenario 1), while in the zone below the line $\Delta L < \Delta G$, and the precipitation increases (scenario 2). The realization of the first or the second scenario depends on the environmental conditions and the cloud type. For instance, if the air humidity is high, the condensate gain is large and the condensate loss is low, which leads to an increase in the precipitation (as, e.g., in tropical deep clouds in dirty air). To show the effect of humidity, clearer supplemental simulations M-80 and M-c-80 have been performed, which differ from the M case and the M-c case, respectively, by a 10% lower humidity over the whole atmosphere (so that the RH at the surface was 80% instead of 90%). The comparison of accumulated rain in the simulations M-, M-c, M80, and M-c-80 (Fig. 13) shows that the decrease in RH leads not only to a dramatic decrease in the precipitation (the cloud-top height decreased to 4.5 km; see Fig. 18), but also to the change of the sign of the precipitation response to aerosols. In other words, while the precipitation in the M-c was larger than that in the M clouds, the precipitation in M-c-80 is smaller than that in the M-80 cloud. Figure 18 shows that in the case of comparatively small cumulus clouds, when the role of cloud ice is negligible, an increase in the aerosol concentration significantly increases the loss of the precipitating mass, so that $\Delta L > \Delta G$.

Note that both ΔG and ΔL depend on the convection structure. Small isolated clouds experience intense mixing with the environment, which increases ΔL. In contrast, large cloud clusters, supercell storms, and squall lines have large ΔG and relatively small ΔL because humidity is high within the convection zone. In these systems, one can expect an increase in precipitation and an increase in the aerosol concentration. These cases are denoted by the corresponding boxes on the scheme in Fig. 17.

Thus, the analysis of the aerosol effects on the water and heat budgets indicates the crucial role of RH in determining the sign of the precipitation response to aerosols. It allows us to attribute the increase in precipitation associated with the increase in the aerosol concentration [reported variously by Shepherd and Burian (2003) for the Houston region, Ohashi and Kida

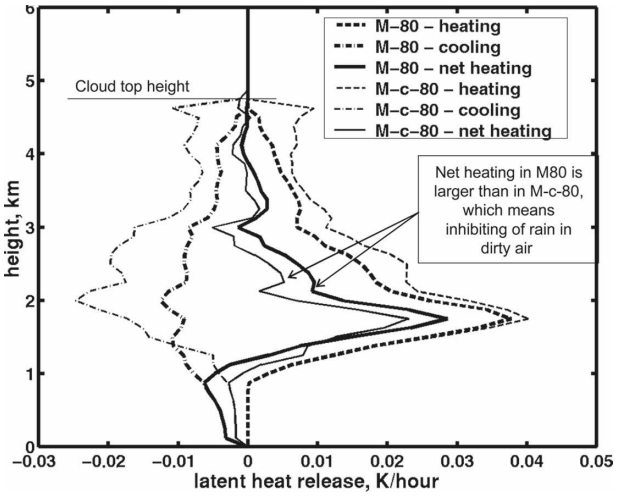

FIG. 18. The same as Fig. 16 but for the M and the M-80 cases. Net heating in the M-80 is higher than in the M-c-80, which indicates a decrease in the precipitation from tropical small cumulus clouds in a comparatively dry atmosphere.

(2002) for the coastal regions of Japan, and Wang (2005) for deep tropical convection] to a high air humidity in the corresponding areas. (These cases are marked by corresponding boxes in the scheme.)

On the other hand, a decrease in precipitation from orographic clouds over the Sierra Nevada (Givati and Rosenfeld 2004), especially over the downwind (easterly) slope of the mountains, can be attributed to the low humidity leading to a dramatically rapid evaporation of the condensate (Lynn et al. 2007). Simulations of both small warm-rain cumulus clouds (as discussed above) and stratocumulus clouds (Magaritz et al. 2007) indicate a high sensitivity of these clouds to aerosols, because an increase in the AP concentration leads to the formation of a large amount of small drops that fall slowly and evaporate much more efficiently than the rapidly falling raindrops. These results explain the decrease in the precipitation from small cumulus and stratocumulus clouds in dirty air reported in many studies (Albrecht 1989; Rosenfeld, 1999, 2000; Rosenfeld and Woodley 2000; Feingold et al. 2005), as well as the inhibition of precipitation in dirty air for an Oklahoma warm cloud system found by Cheng et al. (2007).

To a certain extent these considerations can be also applied to the classification of the results concerning cloud ensembles and squall lines. However, Lynn et al. (2005b) reported an increase in the precipitation rate and the accumulated rain in the zone of the squall line in Florida where the air is quite humid. Recently, Tao et al. (2007) reported an increase in precipitation from the tropical squall line Tropical Ocean and Global Atmosphere Coupled Ocean–Atmosphere Response Experiment (TOGA COARE) and a slight decrease in the precipitation in continental PRESTORM squall line. Thus, many apparent discrepancies between the results reported about the precipitation response to aerosols are delusive, and can be attributed to different atmospheric conditions (particularly to differences in air humidity). High humidity increases the precipitation efficiency, which is especially important in dirty air.

The aerosol effects on precipitation can be categorized as "intensive" (when the difference $\Delta G - \Delta L$ is changed in individual clouds or in single storms) and "extensive" (when the number of clouds is changed). As shown by Khain et al. (2003, 2005), Lynn et al. (2005a), and recently by Lee et al. (2008), clouds forming in dirty air create stronger downdrafts because of higher atmospheric cooling (see Fig. 12). These downdrafts increase the convergence in the boundary layer and foster the formation of secondary clouds, squall lines, etc. These dynamical aerosol effects foster the formation of a larger number of clouds and organized cloud systems. The increase in precipitation in this case is caused mainly by the formation of a larger number of clouds. The dynamical effects of aerosols lead, therefore, to an increase of $\Delta G - \Delta L$ over large areas containing clusters of clouds. However, the increase in the cloud number also increases relative to air humidity, thereby increasing the precipitation because of an increase in $\Delta G - \Delta L$ in individual clouds as well.

Note that the relationship between ΔG and ΔL also depends on other thermodynamic parameters. Among them, the atmospheric instability and the vertical wind shear seem to be of main importance. Instability increases the vertical velocity in clouds and transports more drops to the upper levels, thus increasing both ΔG and ΔL, similar to aerosol effects. This makes the problem of separating aerosol and instability effects more difficult (Williams et al. 2002). The net effect (i.e., $\Delta G - \Delta L$) depends on the environmental humidity.

An increase in boundary layer instability can significantly affect the rate of secondary cloud formation. According to this dynamical mechanism, aerosols can increase precipitation in some regions by increasing the rain production without any change in the precipitation efficiency (as we have seen in the case of P clouds). The wind shear also affects ΔG and ΔL, but its contribution is not unique. As is known, there is an optimum wind shear that produces the maximum convection intensity (e.g., Emanuel 1994). A strong wind shear decreases the convection intensity but increases the condensate loss, because a strong wind transports the condensate far from the original cloud, which increases evaporation and sublimation.

8. Conclusions

A simulation of the dynamics and the microphysics of clouds observed during the LBA–SMOCC campaign, as well as of extremely continental and extremely maritime clouds, is performed using an updated version of the spectral microphysics cloud model HUCM. The improved model reproduces well the DSD measured in situ in clouds developing under different aerosol conditions (green ocean, smoky, and pyroclouds). Simulations indicate that the contents of all types of ice (including graupel and hail) are higher in polluted clouds as compared with those in green-ocean and maritime clouds. A significant amount of LWC at low temperature levels in polluted clouds allows efficient riming of ice crystals and fosters graupel and hail production. Crystal–crystal collisions, as well as collisions of large crystals with small droplets, give rise to aggregate formation. The production of hail in the green-ocean and maritime clouds simulated was negligible. Precipitation in the smoky clouds and in most pyroclouds forms with a significant time delay as compared with the green-ocean clouds. It was shown that aerosols in the smoky and pyroclouds tend to inhibit warm rain, so precipitation is caused by melting ice particles (mainly graupel and hail). At the decaying stage, melted snow contributes to precipitation. The precipitation from the green-ocean and maritime clouds is mostly warm rain. The specific feature of pyroclouds is the existence of a continuous surface forcing that was assumed to be immovable with time in the simulations. Owing to the existence of the wind shear, a wavelike structure of the vertical velocity arises, which gives rise to the formation of several secondary clouds with different droplet concentrations. The precipitation formation scenario depends on the values of the wind shear and on the surface heating. We suppose that in most cases (when heating is not so strong) precipitation takes place from the secondary cloud(s) located tens of kilometers downwind from the nonprecipitating primary cloud, which may create a delusive impression that pyroclouds do not precipitate. In the second scenario, the surface fire creates strong temperature gradients leading to the formation of a significant air vorticity downwind of the main cloud updraft, which results in the formation of a hydrometeor recirculation when some of the melting particles are involved in the cloud updraft. The drops that penetrate cloud updrafts efficiently collect small cloud droplets and produce raindrops that freeze by collisions with ice at comparatively low levels above the freezing level. Thus, according to the results of the simulations, the recirculation leads to the precipitation from clouds containing several thousand droplets per cubic centimeter. The recirculation also leads to an increase in the concentration and the mass of hail and graupel in pyroclouds. The utilization of the 2D geometry may overestimate the recirculation intensity. Thus, 3D simulations and further observations of precipitation from pyroclouds are required for future research.

We would like to make the following comment concerning the effects of aerosols on ice (including graupel and hail) generation and precipitation in clouds. Supplemental simulations (not discussed in the paper) indicate a quite weak dependence of the graupel and hail mass on the rate of the primary crystal formation. As soon as the first crystals form, their collisions with water drops and then the collisions of frozen drops with the remaining liquid drops determine the graupel and hail formation. It is the liquid microstructure of clouds that greatly affects the amount of ice (at least, for clouds containing significantly rimed mass). So, the main mechanism by which aerosols affect cloud ice seems to be the influence of aerosols on droplet concentration and droplet size distribution. Of course, the ice–ice and ice–water collision rates (known with a high uncertainty) play a crucial role in the formation of graupel and hail in cumulus clouds. It is possible that the primary ice nucleation plays a more important role in frontal and stratocumulus clouds.

The mechanisms by which aerosols affect the microphysics and precipitation of warm cloud-base clouds have been investigated by analyzing mass, heat, and moisture budgets. It is shown that polluted clouds in all cases produce a larger mass of condensate because of extra droplet condensation and ice deposition (which corresponds to a larger latent heat release). At the same time, the condensate loss in polluted clouds is also greater than in clean air clouds. Since green-ocean and smoky clouds develop in relatively dry air, the growth of the aerosol concentration increases the aerosol-induced loss of hydrometeor mass to a higher degree than the condensate production. As a result, accumulated rain from S clouds turns out to be smaller than from green-ocean clouds. The response of precipitation of Texas clouds to aerosols is similar to that of smoky clouds. On the contrary, an increase in the aerosol concentration in the relatively stable wet tropical atmosphere increases the condensate generation more than the loss, so precipitation increases. Supplemental simulations indicate that aerosols inhibit precipitation from stratocumulus and small cumulus clouds with the warm cloud base.

Other factors affecting the generation and loss of condensate are instability and wind shear, as well as the structure of the cloud-related phenomena. In the case

of supercell storms and squall lines, precipitation over a large area moistens the air, thereby decreasing the precipitation loss. The results of the budget analysis have been summarized in Fig. 17. The comparison scheme shown there allows us to interpret many discrepancies of the results reported in different studies regarding aerosol effects on precipitation as rather delusive. These discrepancies can be attributed to the differences in the environmental conditions of the observations or numerical simulations, as well as to different types of clouds analyzed. The studies reporting a decrease in the precipitation with an increase in aerosol concentration usually deal with isolated cumulus clouds developing within a relatively dry atmosphere and/or within large wind shears or stratocumulus clouds. The studies reporting an increase in the precipitation often deal with clouds forming in a moist atmosphere, such as coastal zones or within cloud ensembles, tropical squall lines, etc.

Note that the scheme shown in Fig. 17 concerns only the cloud systems formed in the atmosphere with a high (about 4 km or more) freezing level. Such systems produce warm rain in response to low aerosol concentrations and cold precipitation in response to high aerosol concentrations. For such systems the dependence of precipitation on aerosols supposedly is monotonic within a wide range of aerosol concentrations.

Aerosol effects on the clouds with a low freezing level require special investigations. In these clouds warm rain is negligibly small, so cold precipitation is dominant within a wide range of aerosol concentrations. Teller and Levin (2006) showed that high CCN concentrations reduced precipitation in isolated mixed-phase convective clouds with a 2-km-height freezing level. However, these simulations were performed for a period of about 1 h and for two values of CCN concentrations only. Our preliminary simulations of sets of such clouds containing primary and secondary clouds, carried out for a period of 6 h, showed that the dependence of precipitation on aerosols for such clouds may become nonmonotonic with the maximum precipitation at about 500–800 cm^{-3} CCN.

Note that the results obtained in the present study can be changed, at least quantitively, as soon as better knowledge about ice–ice and ice–water collisions becomes available.

As shown in the study, aerosols affect the vertical profiles of convective heating and cooling, which can influence not only the precipitation from single clouds but also the dynamics of mesoscale systems such as tropical cyclones (Zhang et al. 2007; Rosenfeld et al. 2007; Khain et al. 2007). In large complex terrains or coastal regions aerosols can redistribute precipitation, so that precipitation can increase in one place at the expense of a decrease in another place. The net effect can depend on the thermodynamic conditions dominating in one or another geographical zone. Further investigations of different types of clouds and thermodynamic parameters are required to make the presented classification scheme quantitative. Additional efforts are required to develop and utilize 3D mesoscale models with spectral bin microphysics. Further investigations of the relationship between aerosols, instability, and lightning (Williams et al. 2002; Sherwood et al. 2006) are required.

Acknowledgments. This study was supported by the European Grant ANTISTORM, as well as by the Israel Ministry of Science (the Germany–Israel collaboration in Water Resources, Grant W403). The authors are grateful to Prof. A. Bott, who provided codes for the advection of positively defined values as well as valuable comments.

APPENDIX A

Solution of the Equation System for Supersaturations

To take into account the changes of supersaturaion during one time step for diffisional growth, Tzivion et al. (1989), Khain and Sednev (1996), and Khain et al. (2004) solved an equation system for supersaturations with respect to water S_1 and ice S_2 that can be easily derived from the equations for temperature, the mixing ratio, and the Clausius–Clapeyron relationship as follows:

$$\frac{dS_1}{dt} = -P_1 S_1 - P_2 S_2, \quad \text{and} \quad \frac{dS_2}{dt} = -R_1 S_1 - R_2 S_2, \tag{A1}$$

where

$$P_1 = \frac{e}{e_{sw}}\left(a + \frac{L_1 B_1}{c_p T^2}\right)\int_0^\infty f_1 F_1\, dm,$$

$$P_2 = \frac{e}{e_{sw}}\left(a + \frac{L_2 B_1}{c_p T^2}\right)\sum_{i=2}^{7}\int_0^\infty f_i F_i\, dm,$$

$$R_1 = \frac{e}{e_{s,\mathrm{ice}}}\left(a + \frac{L_1 B_2}{c_p T^2}\right)\int_0^\infty f_1 F_1\, dm, \quad \text{and}$$

$$R_2 = \frac{e}{e_{s,\mathrm{ice}}}\left(a + \frac{L_2 B_2}{c_p T^2}\right)\sum_{i=2}^{7}\int_0^\infty f_i F_i\, dm. \tag{A2}$$

In (A2), f_i is the size distribution function of the ith type hydrometeor ($i = 1$ denotes water; $i > 1$ denotes different ice particles), and e, e_{sw}, and $e_{s,\mathrm{ice}}$ are water vapor

pressure and the saturation values of the water vapor pressure over water and ice, respectively. The remaining variables are calculated as $a = 1/[q(0.622 + q)]$, $B_1 = L_1/R_v$, $B_2 = L_2/R_v$, and $F_i = (1/S)(dm_i/dt)$, where R_v is the gas constant of wet air, q is the mixing ratio, and m_i is the mass of particles belonging to the ith type hydrometeor. The initial supersaturations needed for solving (A1) and (A2) are the values S_1^* and S_2^*, obtained after the advection substep. According to (2) in the new method, the following equation system is solved at each time step:

$$\frac{dS_1}{dt} = -P_1S_1 - P_2S_2 + \left[\frac{\delta S_1}{\delta t}\right]_{\text{dyn}}, \quad \text{and}$$

$$\frac{dS_2}{dt} = -R_1S_1 - R_2S_2 + \left[\frac{\delta S_2}{\delta t}\right]_{\text{dyn}}, \tag{A3}$$

where $[\delta S_1/\delta t]_{\text{dyn}}$ and $[\delta S_2/\delta t]_{\text{dyn}}$ are the tendencies of supersaturation values calculated during the dynamical (advective) time step. We consider three cases: (i) there is only liquid water in a spatial grid point, (ii) there is only ice, and (iii) the general case of the mixed phase. The solutions are as follows:

(i) only liquid water

$$\begin{aligned}
S_1(t) &= S_1(0)e^{-P_1t} + \frac{\left[\frac{\delta S_1}{\delta t}\right]_{\text{dyn}}}{P_1}(1 - e^{-P_1t}) \int_0^t S_1(t)\,dt \\
&= \left[\frac{S_1(0)}{P_1} + \frac{\left[\frac{\delta S_1}{\delta t}\right]_{\text{dyn}}}{P_1^2}\right]e^{-P_1t} + \frac{\left[\frac{\delta S_1}{\delta t}\right]_{\text{dyn}}}{P_1}t + \frac{S_1(0)}{P_1} - \frac{\left[\frac{\delta S_1}{\delta t}\right]_{\text{dyn}}}{P_1^2}, \quad \text{and} \\
S_2(t) &= \left[\frac{R_1S_1(0)}{P_1} - \frac{R_1\left[\frac{\delta S_1}{\delta t}\right]_{\text{dyn}}}{P_1^2}\right]e^{-P_1t} - \left(\frac{R_1\left[\frac{\delta S_1}{\delta t}\right]_{\text{dyn}}}{P_1} - \left[\frac{\delta S_2}{\delta t}\right]_{\text{dyn}}\right)t + S_2(0) - \frac{R_1S_1(0)}{P_1} + \frac{R_1\left[\frac{\delta S_1}{\delta t}\right]_{\text{dyn}}}{P_1^2}\int_0^t S_2(t)\,dt \\
&= \left[\frac{R_1S_1(0)}{-P_1^2} - \frac{R_1\left[\frac{\delta S_1}{\delta t}\right]_{\text{dyn}}}{P_1^3}\right]e^{-P_1t} - \left(\frac{R_1\left[\frac{\delta S_1}{\delta t}\right]_{\text{dyn}}}{P_1} - \left[\frac{\delta S_2}{\delta t}\right]_{\text{dyn}}\right)\frac{t^2}{2} + \left[S_2(0) - \frac{R_1S_1(0)}{P_1} + \frac{R_1\left[\frac{\delta S_1}{\delta t}\right]_{\text{dyn}}}{P_1^2}\right]t \\
&\quad + \frac{R_1S_1(0)}{P_1^2} - \frac{R_1\left[\frac{\delta S_1}{\delta t}\right]_{\text{dyn}}}{P_1^3},
\end{aligned} \tag{A4}$$

(ii) only ice

$$\begin{aligned}
S_2(t) &= S_2(0)e^{-R_2} + \frac{\left[\frac{\delta S_2}{\delta t}\right]_{\text{dyn}}}{R_2}(1 - e^{-R_2t}) \int_0^t S_2(t)\,d\tau \\
&= \left[\frac{S_2(t)}{R_2} + \frac{\left[\frac{\delta S_2}{\delta t}\right]_{\text{dyn}}}{R_2^2}\right]e^{-R_2t} + \frac{\left[\frac{\delta S_2}{\delta t}\right]_{\text{dyn}}}{R_2}t + \frac{S_2(t)}{R_2} - \frac{\left[\frac{\delta S_2}{\delta t}\right]_{\text{dyn}}}{R_2^2}, \quad \text{and} \\
S_1(t) &= \left[\frac{P_1S_2(0)}{R_2} - \frac{P_2\left[\frac{\delta S_2}{\delta t}\right]_{\text{dyn}}}{R_2^2}\right]e^{-R_2t} - \left(\frac{P_2\left[\frac{\delta S_2}{\delta t}\right]_{\text{dyn}}}{R_2} - \left[\frac{\delta S_1}{\delta t}\right]_{\text{dyn}}\right)t + S_1(0) - \frac{P_2S_2(0)}{R_2} + \frac{P_2\left[\frac{\delta S_2}{\delta t}\right]_{\text{dyn}}}{R_2^2}\int_o^t S_1(t)\,dt \\
&= \left[\frac{P_2S_2(0)}{-R_2^2} - \frac{P_2\left[\frac{\delta S_2}{\delta t}\right]_{\text{dyn}}}{R_2^3}e^{-R_2t}\right] - \left(\frac{P_2\left[\frac{\delta S_2}{\delta t}\right]_{\text{dyn}}}{R_2} - \left[\frac{\delta S_1}{\delta t}\right]_{\text{dyn}}\right)\frac{t^2}{2} + \left[S_1(0) - \frac{P_2S_2(0)}{R_2} + \frac{P_2\left[\frac{\delta S_2}{\delta t}\right]_{\text{dyn}}}{R_2^2}\right]t \\
&\quad + \frac{P_2S_2(0)}{R_2^2} - \frac{P_2\left[\frac{\delta S_2}{\delta t}\right]_{\text{dyn}}}{R_2^3},
\end{aligned} \tag{A5}$$

(iii) the mixed-phase case

$$S_1(t) = c_{11}e^{\gamma t} + c_{21}e^{-\beta t} + \frac{G_{31}}{G_2}, \quad S_2 = c_{12}e^{\gamma t} + c_{22}e^{-\beta t} + \frac{G_{32}}{G_2}, \quad \int_0^t S_1\,dt = \frac{c_{11}e^{\gamma t}}{\gamma} + \frac{c_{21}e^{-\beta t}}{\beta} + \frac{G_{31}}{G_2}t + \frac{c_{21}}{\beta} - \frac{c_{11}}{\gamma}, \quad \text{and}$$

$$\int_0^t S_2\,dt = \frac{c_{12}e^{\gamma t}}{\gamma} + \frac{c_{22}e^{-\beta t}}{\beta} + \frac{G_{32}}{G_2}t + \frac{c_{22}}{\beta} - \frac{c_{12}}{\gamma}, \tag{A6}$$

where

$$\alpha = \sqrt{(P_1 - R_2)^2 + 4P_2R_1}, \quad \beta = \frac{\alpha + P_1 + R_2}{2}, \quad \gamma = \frac{\alpha - P_1 - R_2}{2},$$

$$c_{11} = \alpha^{-1}\left(\beta\Delta_1 - p_1\Delta_1 - p_2\Delta_2 - \beta\frac{G_{31}}{G_2} + \left[\frac{\delta S_1}{\delta t}\right]_{\text{dyn}}\right),$$

$$c_{12} = \alpha^{-1}\left(\gamma\Delta_1 + p_1\Delta_1 + p_2\Delta_2 - \gamma\frac{G_{31}}{G_2} - \left[\frac{\delta S_1}{\delta t}\right]_{\text{dyn}}\right),$$

$$c_{21} = \alpha^{-1}\left(\beta\Delta_2 - r_1\Delta_1 - r_2\Delta_2 - \beta\frac{G_{32}}{G_2} + \left[\frac{\delta S_2}{\delta t}\right]_{\text{dyn}}\right),$$

$$c_{22} = \alpha^{-1}\left(\gamma\Delta_2 + r_1\Delta_1 + r_2\Delta_2 - \gamma\frac{G_{32}}{G_2} - \left[\frac{\delta S_2}{\delta t}\right]_{\text{dyn}}\right),$$

$$G_1 = P_1 + R_2, \quad G_2 = P_1R_2 - P_2R_1, \quad G_{31} = R_2\left[\frac{\delta S_1}{\delta t}\right]_{\text{dyn}} - P_2\left[\frac{\delta S_2}{\delta t}\right]_{\text{dyn}}, \quad \text{and}$$

$$G_{32} = P_1\left[\frac{\delta S_2}{\delta t}\right]_{\text{dyn}} - R_1\left[\frac{\delta S_1}{\delta t}\right]_{\text{dyn}}.$$

These expressions were used when calculating the diffusional growth of particle mass m_i as shown here:

$$m_t^{t+\Delta t} = m_i^t + F_i\int_t^{t+\Delta t} S(t)\,d\tau. \tag{A7}$$

APPENDIX B

A New Remapping Scheme

Let m_i be the mass drop belonging to the ith bin of a regular mass grid. At one time step of the diffusion growth, mass m_i grows to $m_{i,\text{new}}$, so that the regular mass grid transforms into a nonregular one. To calculate the masses and concentrations of particles (drops or ice particles) at the time step $t + dt$ it is necessary to interpolate the DSD from the nonregular mass grid to the regular one, that is, to perform remapping. The remapping is performed under the conservation of the total concentration (the first moment), the total mass (the third moment), and the radar reflectivity (the sixth moment). Respectively, three equations expressing these conservation laws were solved for each mass bin of the nonregular grid:

$$N_{i,\text{new}} = N_{i-1} + N_i + N_{i+1}, \quad M_{i,\text{new}} = N_{i,\text{new}}m_{i,\text{new}} = M_{i-1} + M_i + M_{i+1} = N_{i-1}m_{i-1} + N_im_i + N_{i+1}m_{i+1}, \quad \text{and}$$

$$Z_{i,\text{new}} = N_{i,\text{new}}m_{i,\text{new}}^2 = Z_{i-1} + Z_i + Z_{i+1} = N_{i-1}m_{i-1}^2 + N_im_i^2 + N_{i+1}m_{i+1}^2, \tag{B1}$$

where $m_{i-1} < m_i < m_{i,\text{new}} < m_{i+1}$. In (B1), $N_{i,\text{new}}$ and N_i are the concentrations of particles in a nonregular mass bin i, new, and the concentration of particles to be added to the ith bin as a result of remapping. The solution of (B1) is

$$N_{i-1} = N_{i,\text{new}} \frac{m_{i+1} - m_{i,\text{new}}}{m_{i+1} - m_{i-1}} \frac{m_i - m_{i,\text{new}}}{m_i - m_{i-1}}, \quad N_i = N_{i,\text{new}} \frac{m_{i+1} - m_{i,\text{new}}}{m_{i+1} - m_i} \frac{m_{i,\text{new}} - m_{i-1}}{m_i - m_{i-1}}, \quad \text{and}$$

$$N_{i+1} = N_{i,\text{new}} \frac{m_i - m_{i,\text{new}}}{m_{i+1} - m_{i-1}} \frac{m_{i,\text{new}} - m_{i-1}}{m_i - m_{i+1}}. \tag{B2}$$

Using the concentrations N_i to be added to the ith bin, one can calculate the mass M_i to be added to this bin as $M_i = N_i m_i$.

REFERENCES

Albrecht, B. A., 1989: Aerosols, cloud microphysics, and fractional cloudiness. *Science,* **245,** 1227–1230.

Andreae, M. O., D. Rosenfeld, P. Artaxo, A. A. Costa, G. P. Frank, K. M. Longlo, and M. A. F. Silva-Dias, 2004: Smoking rain clouds over the Amazon. *Science,* **303,** 1337–1342.

Borys, R. D., D. H. Lowenthal, and D. L. Mitchell, 2000: The relationships among cloud microphysics, chemistry, and precipitation rate in cold mountain clouds. *Atmos. Environ.,* **34,** 2593–2602.

Bott, A., 1989: A positive definite advection scheme obtained by nonlinear renormalization of the advective fluxes. *Mon. Wea. Rev.,* **117,** 1006–1015.

——, 1998: A flux method for the numerical solution of the stochastic collection equation. *J. Atmos. Sci.,* **55,** 2284–2293.

Braham, R. R., 1952: The water and energy budgets of the thunderstorm and their relationship to thunderstorm development. *J. Atmos. Sci.,* **9,** 227–242.

Cheng, C.-T., W.-C. Wang, and J.-P. Chen, 2007: A modeling study of aerosol impacts on cloud microphysics and radiative properties. *Quart. J. Roy. Meteor. Soc.,* **133,** 283–297.

Cofer, W. R., E. L. Winstead, B. J. Stocks, L. W. Overbay, J. D. Goldammer, D. R. Cahoon, and J. S. Levine, 1996: Emissions from boreal forest fires: Are the atmospheric chemical impacts underestimated? *Biomass Burning and Global Change,* Vol. 2, J. S. Levine, Ed., MIT Press, 834–839.

Dennis, A. S., and D. J. Musil, 1973: Calculation of hailstone growth and trajectories in a simple cloud model. *J. Atmos. Sci.,* **30,** 278–288.

Eagan, R. C., P. V. Hobbs, and L. F. Radke, 1974: Measurements of cloud condensation nuclei and cloud droplet size distributions in the vicinity of forest fires. *J. Appl. Meteor.,* **13,** 553–557.

Emanuel, K. A., 1994: *Atmospheric Convection*. Oxford University Press, 580 pp.

Feingold, G., H. Jiang, and J. Y. Harrington, 2005: On smoke suppression of clouds in Amazonia. *Geophys. Res. Lett.,* **32,** L02804, doi:10.1029/2004GL021369.

Ferrier, B. S., and R. A. Houze, 1989: One-dimensional time-dependent modeling of GATE cumulonimbus convection. *J. Atmos. Sci.,* **46,** 330–352.

——, J. Simpson, and W.-K. Tao, 1996: Factors responsible for precipitation efficiencies in midlatitude and tropical squall simulations. *Mon. Wea. Rev.,* **124,** 2100–2125.

Forster, C., and Coauthors, 2001: Transport of boreal forest fire emissions from Canada to Europe. *J. Geophys. Res.,* **106,** 22 887–22 906.

Fromm, M. D., and R. Servranckx, 2003: Transport of forest fire smoke above the tropopause by supercell convection. *Geophys. Res. Lett.,* **30,** 1542, doi:10.1029/2002GL016820.

Givati, A., and D. Rosenfeld, 2004: Quantifying precipitation suppression due to air pollution. *J. Appl. Meteor.,* **43,** 1038–1056.

Hallett, J., and S. C. Mossop, 1974: Production of secondary ice particles during the riming process. *Nature,* **249,** 26–28.

Heymsfield, G. M., and S. Schotz, 1985: Structure and evolution of a severe squall line over Oklahoma. *Mon. Wea. Rev.,* **113,** 1563–1589.

Hobbs, P. V., T. J. Matejka, P. H. Herzegh, J. D. Locatelli, and R. A. Houze, 1980: The mesoscale and microscale structure and organization of clouds and precipitation in midlatitude cycles. I: A case study of a cold front. *J. Atmos. Sci.,* **37,** 568–596.

Jirak, I. L., and W. R. Cotton, 2006: Effect of air pollution on precipitation along the front range of the Rocky Mountains. *J. Appl. Meteor. Climatol.,* **45,** 236–245.

Jost, H.-J., K. Drdla, A. Stohl, L. Pfister, M. Loewenstein, and J. P. Lopez, 2004: In-situ observations of mid-latitude forest fire plumes deep in the stratosphere. *Geophys. Res. Lett.,* **31,** L11101, doi:10.1029/2003GL019253.

Khain, A. P., 2006: Aerosol effects on microphysics and precipitation: Classification of numerical results. *Proc. AGU 2006 Fall Meeting,* San Francisco, CA, Amer. Geophys. Union.

——, and I. Sednev, 1996: Simulation of precipitation formation in the eastern Mediterranean coastal zone using a spectral microphysics cloud ensemble model. *Atmos. Res.,* **43,** 77–110.

——, and A. Pokrovsky, 2004: Simulation of effects of atmospheric aerosols on deep turbulent convective clouds using a spectral microphysics mixed-phase cumulus cloud model. Part II: Sensitivity study. *J. Atmos. Sci.,* **61,** 2983–3001.

——, M. Ovtchinnikov, M. Pinsky, A. Pokrovsky, and H. Krugliak, 2000: Notes on the state-of-the-art numerical modeling of cloud microphysics. *Atmos. Res.,* **55,** 159–224.

——, M. B. Pinsky, M. Shapiro, and A. Pokrovsky, 2001a: Collision rate of small graupel and water drops. *J. Atmos. Sci.,* **58,** 2571–2595.

——, D. Rosenfeld, and A. Pokrovsky, 2001b: Simulating convective clouds with sustained supercooled liquid water down to −37.5°C using a spectral microphysics model. *Geophys. Res. Lett.,* **28,** 3887–3890.

——, ——, and ——, 2003: Simulation of aerosol effects on convective clouds developed under continental and maritime conditions. *Geophysical Research Abstracts,* Vol. 5, Abstract 03180.

——, A. Pokrovsky, M. Pinsky, A. Seifert, and V. Phillips, 2004: Simulation of effects of atmospheric aerosols on deep turbulent convective clouds using a spectral microphysics mixed-phase cumulus cloud model. Part I: Model description. *J. Atmos. Sci.,* **61,** 2963–2982.

——, D. Rosenfeld, and A. Pokrovsky, 2005: Aerosol impact on the dynamics and microphysics of deep convective clouds. *Quart. J. Roy. Meteor. Soc.,* **131,** 2639–2663.

——, N. Cohen, Y. Segal, B. Lynn, D. Rosenfeld, 2007: Effects of aerosols on lightning and structure of tropical cyclones. *Proc. IUGG XXIV,* Perugia, Italy, International Association of Meteorology and Atmospheric Sciences, 986.

Kogan, Y., 1991: The simulation of a convective cloud in a 3-D model with explicit microphysics. Part I: Model description and sensitivity experiments. *J. Atmos. Sci.,* **48,** 1160–1189.

Koren, I., Y. J. Kaufman, D. Rosenfeld, L. A. Remer, and Y. Rudich, 2005: Aerosol invigoration and restructuring of Atlantic convective clouds. *Geophys. Res. Lett.,* **32,** L14828, doi:10.1029/2005GL023187.

Kovetz, A., and B. Olund, 1969: The effect of coalescence and condensation on rain formation in a cloud of finite vertical extent. *J. Atmos. Sci.,* **26,** 1060–1065.

Kuba, N., and Y. Fujiyoshi, 2006: Development of a cloud microphysical model and parameterizations to describe the effect of CCN on warm cloud. *Atmos. Chem. Phys.,* **6,** 2793–2810.

Lee, S., L. Donner, and V. Phillips, 2008: Impact of aerosols on precipitation in deep convection. *Quart. J. Roy. Meteor. Soc.,* in press.

Li, X., C.-H. Sui, and K.-N. Lau, 2002: Precipitation efficiency in the tropical deep convective regime: A 2-D cloud resolving modeling study. *J. Meteor. Soc. Japan,* **80,** 205–212.

Liu, Q., Y. Kogan, and D. K. Lilly, 1995: Reducing the numerical dispersion of the cloud droplet spectrum in condensation calculations. Preprints, *Conf. on Cloud Physics,* Dallas, TX, Amer. Meteor. Soc., 112–117.

Lynn, B. H., A. Khain, J. Dudhia, D. Rosenfeld, A. Pokrovsky, and A. Seifert, 2005a: Spectral (bin) microphysics coupled with a mesoscale model (MM5). Part I: Model description and first results. *Mon. Wea. Rev.,* **133,** 44–58.

——, ——, ——, ——, ——, and ——, 2005b: Spectral (bin) microphysics coupled with a mesoscale model (MM5). Part II: Simulation of a CaPE rain event with squall line. *Mon. Wea. Rev.,* **133,** 59–71.

——, ——, D. Rosenfeld, and W. Woodley, 2007: Effects of aerosols on precipitation from orographic clouds. *J. Geophys. Res.,* **112,** D10225, doi:10.1029/2006JD007537.

Magaritz, L., M. Pinsky, and A. Khain, 2007: Drizzle formation in stratocumulus clouds. *Proc. IUGG XXIV,* Perugia, Italy, International Association of Meteorology and Atmospheric Sciences, 872.

Marwitz, J. D., 1972: Precipitation efficiency of thunderstorms on the high plains. *J. Rech. Atmos.,* **6,** 367–370.

Meyers, M. P., P. J. DeMott, and W. R. Cotton, 1992: New primary ice-nucleation parameterizations in an explicit cloud model. *J. Appl. Meteor.,* **31,** 708–721.

Ohashi, Y., and H. Kida, 2002: Local circulations developed in the vicinity of both coastal and inland urban areas: A numerical study with a mesoscale atmospheric model. *J. Appl. Meteor.,* **41,** 30–45.

Phillips, V., A. Pokrovsky, and A. Khain, 2007: The influence of time-dependent melting on the dynamics and precipitation production in maritime and continental storm clouds. *J. Atmos. Sci.,* **64,** 338–359.

Pinsky, M., and A. P. Khain, 1998: Some effects of cloud turbulence on water–ice and ice–ice collisions. *Atmos. Res.,* **47–48,** 69–86.

——, and ——, 2002: Effects of in-cloud nucleation and turbulence on droplet spectrum formation in cumulus clouds. *Quart. J. Roy. Meteor. Soc.,* **128,** 501–533.

——, ——, and M. Shapiro, 1999: Collisions of small drops in a turbulent flow. Part I: Collision efficiency. Problem formulation and preliminary results. *J. Atmos. Sci.,* **56,** 2585–2600.

——, ——, and ——, 2000: Stochastic effects of cloud droplet hydrodynamic interaction in a turbulent flow. *Atmos. Res.,* **53,** 131–169.

——, ——, and ——, 2001: Collision efficiency of drops in a wide range of Reynolds numbers: Effects of pressure on spectrum evolution. *J. Atmos. Sci.,* **58,** 742–764.

Pruppacher, H. R., 1995: A new look at homogeneous ice nucleation in supercooled water drops. *J. Atmos. Sci.,* **52,** 1924–1933.

——, and J. D. Klett, 1997: *Microphysics of Clouds and Precipitation.* 2nd ed. Oxford University Press, 963 pp.

Ramanathan, V., P. J. Crutzen, J. T. Kiehl, and D. Rosenfeld, 2001: Aerosols, climate, and the hydrological cycle. *Science,* **294,** 2119–2124.

Rissler, J., E. Swietlicki, J. Zhou, G. Roberts, M. O. Andreae, L. V. Gatti, and P. Artaxo, 2004: Physical properties of the sub-micrometer aerosol over the Amazon rain forest during the wet-to-dry season transition—Comparison of modeled and measured CCN concentrations. *Atmos. Chem. Phys.,* **4,** 2119–2143.

Rosenfeld, D., 1999: TRMM observed first direct evidence of smoke from forest fires inhibiting rainfall. *Geophys. Res. Lett.,* **26** (20), 3105–3108.

——, 2000: Suppression of rain and snow by urban and industrial air pollution. *Science,* **287,** 1793–1796.

——, and I. M. Lensky, 1998: Spaceborne sensed insights into precipitation formation processes in continental and maritime clouds. *Bull. Amer. Meteor. Soc.,* **79,** 2457–2476.

——, and W. L. Woodley, 2000: Deep convective clouds with sustained supercooled liquid water down to −37.5°C. *Nature,* **405,** 440–442.

——, A. Khain, B. Lynn, and W. L. Woodley, 2007: Simulation of hurricane response to suppression of warm rain by submicron aerosols. *Atmos. Chem. Phys. Discuss.,* **7,** 3411–3424.

Segal, Y., and A. Khain, 2006: Dependence of droplet concentration on aerosol conditions in different cloud types: Application to droplet concentration parameterization of aerosol conditions. *J. Geophys. Res.,* **111,** D15204, doi:10.1029/2005JD006561.

Shepherd, J. M., and S. J. Burian, 2003: Detection of urban-induced rainfall anomalies in a major coastal city. *Earth Interactions,* **7.** [Available online at http://EarthInteractions.org.]

Sherwood, S. C., V. Phillips, and J. S. Wettlaufer, 2006: Small ice crystals and the climatology of lightning. *Geophys. Res. Lett.,* **33,** L05804, doi:10.1029/2005GL025242.

Smith, P. L., D. J. Musil, A. G. Detwiler, and R. Ramachandran, 1999: Observations of mixed-phase precipitation within a CaPE thunderstorm. *J. Appl. Meteor.,* **38,** 145–155.

Sui, C.-S., X. Li, and M.-J. Yang, 2007: On the definition of precipitation efficiency. *J. Atmos. Sci.,* **64,** 4506–4513.

Takahashi, T., T. Endoh, G. Wakahama, and N. Fukuta, 1991: Vapor diffusional growth of free-falling snow crystals between −3 and −23°C. *J. Meteor. Soc. Japan,* **69,** 15–30.

Tao, W.-K., X. Li, A. Khain, T. Matsui, S. Lang, and J. Simpson, 2007: The role of atmospheric aerosol concentration on deep convective precipitation: Cloud-resolving model simulations. *J. Geophys. Res.,* **112,** D24S18, doi:10.1029/2007JD008728.

Teller, A., and Z. Levin, 2006: The effects of aerosols on precipitation and dimensions of subtropical clouds: A sensitivity study using a numerical cloud model. *Atmos. Chem. Phys.,* **6,** 67–80.

Tzivion, S., G. Feingold, and Z. Levin, 1989: The evolution of raindrop spectra. Part II: Collisional collection/breakup and evaporation in a rainshaft. *J. Atmos. Sci.,* **46,** 3312–3327.

Vali, G., 1975: Remarks on the mechanism of atmospheric ice

nucleation. *Proc. Eighth Int. Conf. on Nucleation,* Leningrad, U.S.S.R., Gidrometeoizdat, 265–269.

—— 1994: Freezing rate due to heterogeneous nucleation. *J. Atmos. Sci.,* **51,** 1843–1856.

Van den Heever, S. C., G. G. Carrió, W. R. Cotton, P. J. DeMott, and A. J. Prenni, 2006: Impacts of nucleating aerosol on Florida storms. Part I: Mesoscale simulations. *J. Atmos. Sci.,* **63,** 1752–1775.

Wang, C., 2005: A modelling study of the response of tropical deep convection to the increase of cloud condensational nuclei concentration: 1. Dynamics and microphysics. *J. Geophys. Res.,* **110,** D21211, doi:10.1029/2004JD005720.

Warner, C., J. Simpson, G. V. Helvoirt, D. W. Martin, D. Suchman, and G. L. Austin, 1980: Deep convection on day 261 of GATE. *Mon. Wea. Rev.,* **108,** 169–194.

Williams, E., and Coauthors, 2002: Contrasting convective regimes over the Amazon: Implications for cloud electrification. *J. Geophys. Res.,* **107,** 8082, doi:10.1029/2001JD000380.

Wotawa, G., and M. Trainer, 2000: The influence of Canadian forest fires on pollutant concentrations in the United States. *Science,* **288,** 324–328.

Zhang, H., G. M. McFarquhar, S. M. Saleeby, and W. R. Cotton, 2007: Impacts of Saharan dust as CCN on the evolution of an idealized tropical cyclone. *Geophys. Res. Lett.,* **34,** L14812, doi:10.1029/2007GL029876.